

Raman spectroscopy based measurements of carrier concentration in n-type GaN nanowires grown by plasma-assisted molecular beam epitaxy ¹

L. H. Robins,² E. Horneber,² N. A. Sanford,³ K. A. Bertness,³ M. D. Brubaker,³ and J. B. Schlager³

² *NIST, Applied Chemicals and Materials Division, Boulder, Colorado 80305, USA*

³ *NIST, Applied Physics Division, Boulder, Colorado 80305, USA*

ABSTRACT

The carrier concentration in as-grown ensembles of n-type GaN nanowires was determined by Raman spectroscopy of the coupled longitudinal phonon – plasmon (LPP+) mode, and modeling of the carrier concentration dependence of the LPP+ frequency. The Raman measurements and analyses enabled estimation of the carrier concentration in single-nanowire devices fabricated from the as-grown ensembles. The nanowires were grown by plasma-assisted molecular beam epitaxy in either of two growth systems. Twelve samples were examined, of which 11 samples were Si-doped and one was undoped. The Raman-measured carrier concentrations in the Si-doped samples ranged from $(5.28 \pm 1.19) \times 10^{16} \text{ cm}^{-3}$ to $(6.16 \pm 0.35) \times 10^{17} \text{ cm}^{-3}$. For a subset of samples grown with varying Si cell temperature, from 1125 °C to 1175 °C, the carrier concentration was found to be an Arrhenius function of Si cell temperature, with activation energy of $6.281 \pm 0.011 \text{ eV}$. Co-illumination by an above band gap UV laser (325 nm, excitation intensity = 0.7 W/cm² or 4.5 W/cm²) induced small increases in carrier concentration, relative to illumination by the Raman excitation laser alone (633 nm, excitation intensity $\approx 100 \text{ kW/cm}^2$). The lowest Si-doped sample showed the largest increase in

¹ Contribution of NIST, an agency of the US government; not subject to copyright in the United States.

carrier concentration, $(6.3 \pm 4.8) \times 10^{15} \text{ cm}^{-3}$ with UV excitation intensity of 0.7 W/cm^2 . These results imply that, even in the absence of UV illumination, surface depletion does not have a significant effect on the Raman carrier concentration measurements. Immersion in a high-dielectric-constant oil ($\epsilon=2.24$) caused downshifts of similar magnitude in the LPP+ frequencies of undoped and doped nanowires. This result implies that the LPP+ mode has bulk plasmon rather than surface plasmon character, because immersion in a high-dielectric-constant medium is predicted to cause a large decrease in the surface plasmon frequency, which would induce a larger LPP+ downshift in doped than undoped nanowires. A surface optical (SO) phonon peak was observed in each sample in air at $\approx 96.4\%$ of the LPP+ frequency. The SO frequency decreased to $\approx 93.1\%$ of the LPP+ frequency upon oil immersion, as predicted by a simple dielectric model.

I. INTRODUCTION

Measurements of fundamental electrical transport properties of n-type or p-type doped semiconductor nanowires (NWs), including carrier concentration, carrier mobility, and surface depletion and band-bending, are needed as inputs for design, modeling, and performance analysis of devices. Nanowires made of GaN and related III-nitride materials show great promise for single-NW device applications including FETs, light-emitting diodes, and laser diodes.^{1,2} The electrical measurement methods commonly used to quantify carrier concentration and mobility in bulk and thin-film semiconductors, including Hall effect and capacitance-voltage, cannot readily be applied to NWs because of their quasi-one-dimensional geometry.

Coupling between the Raman-active longitudinal optical (LO) phonon modes and plasmon oscillations of the free-carrier “gas” in a polar semiconductor gives rise to Raman-

active coupled phonon-plasmon modes, denoted the LPP– mode (below the uncoupled LO phonon frequency) and LPP+ mode (above the uncoupled LO phonon frequency).^{3,4} The LPP+ frequency increases with carrier concentration, thus enabling a contactless, local, optical probe of carrier concentration, as first shown³ for GaP and other bulk semiconductors with the zincblende structure. Raman spectroscopy has been used to measure the carrier concentration in n-type wurtzite-structure GaN materials, including NWs^{5,6}, epilayers^{7,8}, and free-standing single crystals^{9,10}, as well as InN NWs¹¹.

In related work on optical characterization of electrical transport properties of III-V semiconductor NWs, the photo-generated carrier density and carrier mobility¹² in GaN NW ensembles (grown at NIST) was measured by optical-pump terahertz-probe (OPTP) spectroscopy, which can be described as a non-contact photoconductivity technique. Subsequently, the carrier density and mobility in modulation-doped GaAs/AlGaAs core-shell NWs¹³ was measured by OPTP spectroscopy. (For comparison to the other techniques discussed in the study, note that the spatial resolution of the OPTP technique is limited by the THz probe beam diameter¹³ of ≈ 1 mm.) Forward-scattering (transmission mode) Raman spectroscopy was used to measure the carrier density and mobility in p-type GaAs NWs,¹⁴ based on frequency shifts of the coupled LO-phonon-plasmon modes. A photoluminescence (PL) mapping technique, based on a combination of excitation-intensity-dependent and time-resolved PL measurements, provided spatially resolved measurements of the carrier concentration and non-radiative lifetime along the length of single Si-doped InP NWs.¹⁵ Application of the PL technique requires that the surface recombination rate of the photo-generated carriers is small compared to the bulk radiative and non-radiative recombination rates (which holds for InP but not for GaN), and also requires prior knowledge of the radiative recombination rate constant.

The focus of this study is Raman measurements of the LPP+ mode in ensembles of GaN NWs grown by plasma-assisted molecular beam epitaxy (MBE). MBE-grown GaN NWs have unique properties¹ (as compared to NWs produced by other growth methods), including low residual strain, exclusion of extended defects, long minority carrier and exciton lifetimes, and low surface recombination velocity, which are advantageous for device applications. Samples from a number of growth runs with differing Si doping levels were characterized. Several effects were investigated that can modify the measured LPP+ frequency, and thus complicate the determination of carrier concentration from the Raman data:

- (a) mixing of different LO phonon modes due to light scattering in the NW ensembles;
- (b) possible occurrence of a surface depletion layer;
- (c) presence in some samples of GaN material with non-NW morphology;
- (d) possible surface-plasmon character of the LPP+ mode.

In addition, a Raman-active surface optical (SO) phonon mode was observed, at a frequency approximately 30 cm^{-1} below the LPP+ frequency. The SO mode frequency was observed to upshift with carrier concentration at approximately the same rate as the LPP+ frequency, which suggests that similar phonon-plasmon coupling occurs for the SO mode and the LPP+ mode.

While Raman carrier concentration measurements of single GaN NWs (as opposed to as-grown ensembles of NWs) would be useful, especially when electrical devices are fabricated from single NWs, our instrumentation lacked the sensitivity to quantify LPP+ frequencies and hence carrier concentrations in single NWs. There have been a few Raman spectroscopy studies of single, isolated III-nitride NWs. The strain distribution in an AlGaIn/GaN core-shell NW was measured by resonant Raman spectroscopy¹⁶ with excitation at 353 nm (3.51 eV). Polarized confocal Raman spectroscopy, with incident (or scattered) polarization either parallel or

perpendicular to the 0001 crystal axis, was used to obtain information about the crystalline phase, growth direction, and crystallographic orientation¹⁷ of single GaN NWs. A more detailed discussion of the feasibility of Raman carrier concentration measurements of single NWs is given in the Experimental Results section.

Some preliminary results of this study were presented in an earlier publication on photoconductivity and electronic transport properties of single-NW devices.¹⁸

II. MODEL FOR RAMAN MEASUREMENTS OF CARRIER CONCENTRATION

A. Coupled phonon-plasmon frequencies

The frequencies of the upper-branch (LPP+) and lower-branch (LPP-) coupled phonon-plasmon modes are given^{8,10} by the equation

$$\nu_{LPP\pm}^2 = \frac{1}{2} \left\{ \nu_{LO}^2 + \nu_P^2 \pm \sqrt{(\nu_{LO}^2 + \nu_P^2)^2 - 4\nu_P^2 \nu_{TO}^2} \right\}, \quad (1)$$

with

$$\nu_P = \frac{1}{2\pi c} \left(\frac{Ne^2}{m^* m_e \epsilon_\infty \epsilon_0} \right)^{\frac{1}{2}} = \left(\frac{N}{K m^* \epsilon_\infty} \right)^{\frac{1}{2}}. \quad (2)$$

The constant K is defined as

$$K = \frac{m_e \epsilon_0 (2\pi c)^2}{e^2} = 1.115 \times 10^{15} \text{ m}^{-1}. \quad (3)$$

In Eqs. (1) and (2), ν_{LPP+} and ν_{LPP-} are, respectively, the LPP+ and LPP- frequencies, ν_{LO} is the longitudinal optical phonon frequency, ν_{TO} is the transverse optical phonon frequency, ν_P is the plasmon frequency, N is the carrier concentration, e is the electron charge, m_e is the free electron mass, m^* is the relative (dimensionless) electron effective mass, ϵ_0 is the permeability

of free space, ϵ_∞ is the relative (dimensionless) high-frequency dielectric constant, and c is the speed of light in vacuum. The phonon and plasmon frequencies are expressed in dimensions of reduced wavenumber ($\nu = \omega/2\pi c$, where ω is the angular frequency in radian/s).

In this study, ν_{LPP+} is measured by Raman spectroscopy, and N is then calculated. It is thus helpful to express N as a function of ν_{LPP+} , by inversion of the LPP+ branch of Eq. (1):

$$N(\nu_{LPP+}) = Km^*\epsilon_\infty\nu_P^2 = Km^*\epsilon_\infty \frac{\nu_{LPP+}^2(\nu_{LPP+}^2 - \nu_{LO}^2)}{(\nu_{LPP+}^2 - \nu_{TO}^2)}. \quad (4)$$

While Eq. (1) and Eq. (4) are different forms of the same equation, a useful distinction can be made between these expressions. When considering physical “cause and effect”, the plasmon frequency is a function of the carrier concentration, and ν_{LPP+} is a function of the plasmon frequency; thus, Eq. (1) better describes the physical system. On the hand, when analyzing the experimental results, N is treated as a function of the independent (measured) variable ν_{LPP+} ; thus, Eq. (4) better describes the data analysis. In addition, Eq. (4) is the basis for calculation of the uncertainty of N , as discussed in the Appendix part 3.

A linear approximation to Eq. (4) is reasonably accurate for low N and small LPP+ frequency shift ($\nu_{LPP+} - \nu_{LO} \ll \nu_{LO}$):

$$N \approx P(\nu_{LPP+} - \nu_{LO}) \quad (5a)$$

where

$$P = Km^*\epsilon_\infty \frac{2\nu_{LO}^3}{(\nu_{LO}^2 - \nu_{TO}^2)} \quad (5b)$$

For the most highly doped sample in this study, with calculated $N = 6.16 \times 10^{17} \text{ cm}^{-3}$, the value of N obtained from Eq. (5) is 4.2 % smaller than the exact solution given by Eq. (4).

The above equations assume the use of SI units. However, Raman frequencies and carrier concentrations are commonly expressed in units of cm^{-1} and cm^{-3} , respectively. To use Eq. (4) or (5) in this case, the numerical values of the input parameters ν_{LO} , ν_{TO} , and ν_{LPP+} should be multiplied by a factor of 10^2 (to convert from cm^{-1} to m^{-1}), then the calculated value of N should be multiplied by 10^{-6} (to convert from m^{-3} to cm^{-3}). Or, equivalently, the right-hand side of Eq. (4) or Eq. (5a) should be multiplied by a factor of 10^{-2} .

The LPP+ mode, with $\nu_{LPP+} \geq \nu_{LO}$, was observed for all samples in this study, while the LPP− mode was not observed. The low-frequency cutoff of our spectrometer was $\approx 120 \text{ cm}^{-1}$. The predicted value of ν_{LPP-} is above this cutoff for only two of the examined samples, D273 (125 cm^{-1}) and D270 (167 cm^{-1}). We expect that the LPP− mode would not be observable in our samples, even with a lower cutoff frequency, because of its plasmon-like character. (In the limit $\nu_P \ll \nu_{LO}$, the LPP− branch is plasmon-like and the LPP+ branch is phonon-like.) Plasmon-like modes are generally not observable by Raman spectroscopy because of their small scattering cross-sections. The following statement is made in Ref. 3: “Fig. 4 shows the coupled phonon-plasmon modes ... for three plasmon frequencies ... For low ω_P , the lower mode with frequency ω_- practically disappears”.

In contrast, the LPP− mode was observed by Raman spectroscopy while the LPP+ mode was not observed by Raman in a recent study of undoped, Si doped (n-type), and Mg doped (nominally p-type) InN NWs.¹¹ The frequency shift of the LPP− mode was used to calculate the carrier concentration in these samples. The observation of the LPP− mode was attributed to electric-field induced resonant scattering in the surface accumulation layer. (InN nanomaterials exhibit a large surface electron accumulation layer, unlike GaN, which generally exhibits surface depletion.)

B. Material properties parameters needed to determine carrier concentration

From a data review¹⁹ of band structure parameters for nitrogen-containing compound semiconductors, the electron effective mass of wurtzite-structure GaN (expressed as a ratio to the electron mass in vacuum) is $m^* = 0.20 \pm 0.01$. This is the “bare” or “band curvature” effective mass. The “dressed” or electron-polaron effective mass, which is measured in most experiments, is slightly larger (0.22 to 0.23). The plasmon frequency depends on the bare effective mass.³

The high-frequency dielectric constant, ϵ_∞ , was found to be 5.23 ± 0.1 by extrapolation to long wavelength (low frequency) of previous^{20,21} measurements of the dispersion of the ordinary and extraordinary refractive indices at visible and near-visible wavelengths; details are given in the Appendix part 4. Consideration of the relevant frequency ranges shows that it is reasonable to estimate ϵ_∞ from the low-frequency extrapolation of the refractive index data. More specifically, the dielectric function has the value ϵ_∞ in some range above the (highest) LO phonon frequency, which is 741 cm^{-1} in wurtzite-GaN,²² while the refractive index dispersion was measured at frequencies between 4000 cm^{-1} and 27000 cm^{-1} (i.e., wavelengths between 370 nm and 2500 nm) in Refs. 20 and 21.

The effective LO and TO phonon frequencies (in the absence of phonon-plasmon coupling) were found to be $\nu_{LO} = (739.10 \pm 0.02) \text{ cm}^{-1}$ and $\nu_{TO} = (549.79 \pm 0.02) \text{ cm}^{-1}$. The methods for determination of the LO and TO frequencies will be discussed below.

From the above parameter values and uncertainties, the value and uncertainty of the prefactor P in the linearized expression for N (Eq. 5) is $P = (3.86 \pm 0.21) \times 10^{16} \text{ cm}^{-2}$. Note that all uncertainties in this study are expanded uncertainties that correspond to 95 % confidence intervals.

III. EXPERIMENTAL PROCEDURE

A. MBE growth process

All samples were grown on 76.2 mm (3 inch) diameter Si (111) substrates in one of two growth systems, designated here as the BC system and the D system in order to match the run numbers used in the text (e.g., in Table I). (Note that the same run numbers are used to identify these samples in other publications, such as Ref. 18, to facilitate comparison of the results of different characterization methods.) The nucleation and growth of NWs in these systems occurs without the presence of catalyst nanoparticles and is thus referred to as spontaneous; details of the spontaneous growth mechanism were discussed previously.²³ The primary growth parameters of the samples in this study are given in Table I; the morphologies of the D samples and one of the BC samples (B982) are shown in Fig. 1.

NW growth was nucleated by depositing a few monolayers of Al, striking the plasma source, and then growing an AlN buffer layer approximately 40 nm thick. In the BC system, NWs were nucleated at the lower Ga flux (equivalent to 65 nm/h planar growth), and either grown at that flux the entire run, or if a higher flux is indicated in Table I, the flux was increased after roughly 15 h of growth. Typical growth times were between 72 and 90 h. In the D system, a thin GaN buffer layer was grown on top of the AlN buffer at 670 °C, followed by NW nucleation at final growth temperature. For all the runs except D270, an expansion step was inserted after the first two hours of growth in which the substrate temperature was lowered to 670 °C for approximately one hour with the intent of increasing the NW diameter. As can be seen in Fig. 1, omitting the expansion step for sample D270 does not have a dramatic effect on

NW morphology, though this change in growth conditions may have contributed to the observed increase in carrier concentration for D270 relative to D273.

The N₂ plasma source in the BC system had a single large aperture approximately 1.5 mm in diameter, and its radio-frequency (RF) power was tuned manually for minimal reflection. The N₂ plasma source in the D system had a showerhead aperture designed by the manufacturer for uniform flux and was equipped with an automatic RF tuner. The Ga source flux in the BC system were calibrated with GaAs reflection high energy electron diffraction (RHEED) intensity oscillations, using crystal lattice parameters to convert GaAs monolayers to equivalent GaN monolayers. The N flux was not measured directly in this system, which has since been decommissioned, but we later noted that the growth rate for NWs only increased 1.5× when the Ga flux was increased by a factor of 2.6, from which we conclude that the growth was Ga-limited at the lower flux and likely to be N-limited at the higher flux. Although GaAs runs were also performed in the BC system, we did not observe any indication of As contamination (such as blue photoluminescence²⁴) other than the absence of a 7×7 reconstruction when cooling the Si substrate after an outgas step at approximately 900 °C. The Ga and N source fluxes in the D system were calibrated with growth rate (GR) measurements during planar GaN growth on GaN/sapphire templates. A commercial system that collects white light interference patterns was used to measure layer thickness as a function of time. The fluxes were adjusted to span N-limited to Ga-limited growth at plasma conditions of 1 sccm flow and 300 W. This transition is also characterized by a streaky-to-spotty transition in the RHEED patterns. The Ga fluxes in Table I were calculated using linear extrapolation of the growth rates based on Ga beam equivalent pressure measurements. The N fluxes were estimated by assuming that the effective N species concentration is linearly proportional to both the N₂ flow and the RF power, as indicated

by measurements under two similar N₂ plasma conditions. In this system, the Si (7×7) transition was routinely observed at 830 °C while cooling down from an outgas step at 910 °C. The Si flux could not be measured directly in growth system BC, and it should be noted that the cell was replaced and refilled between runs C023 and C144. In system D, the Si beam equivalent pressure at the highest temperature of 1175 °C was barely detectable at about 3×10^{-11} Torr (4×10^{-9} Pa), approximately 0.002× less than the Ga beam equivalent pressure. The substrate temperatures were measured with a back-side pyrometer²⁵ with an estimated absolute uncertainty of 8 °C. System D displayed a decrease in substrate temperature of about 30 °C from the center to 30 mm from the center along a substrate radius, leading to significant variation in NW growth rate due to Ga re-evaporation. Growth temperatures in Table I were corrected for this variation.

B. Raman spectroscopy

Raman measurements were performed at ambient temperature, approximately 295 K. The Raman scattering was excited by a HeNe laser with a wavelength of 632.822 nm, as determined by calibration with spectral lines of a Ne atomic vapor lamp. The laser beam was focused on the sample by a Mitutoyo M Plan Apo SL 50X microscope objective²⁶ with numerical aperture of 0.42, effective focal length of 4 mm, and working distance of 20.5 mm. The laser beam was expanded (by optical components before the objective) to slightly overfill the entrance pupil of the microscope objective. From a Gaussian beam optics calculation, the focused laser spot diameter is estimated to be 1.0 μm. However, the laser was incident on the sample surface at an angle of 65 ° to normal incidence, which should produce an elliptical spot with estimated size of 2.4 μm × 1.0 μm. The laser power incident on the sample was between 1.2 mW and 7 mW for all experiments (the incident power was controlled by inserting or

removing neutral density filters in the beam path). The excitation intensity was thus estimated to lie between 65 kW/cm^2 and 370 kW/cm^2 . The Raman frequencies and line shapes were observed to be independent of excitation intensity within this range. A polarization rotator in the incident light path enabled selecting either p-polarized (in the plane of incidence) or s-polarized incident light, and a polarization rotator and analyzer in the scattered light path enabled observing either p-polarized or s-polarized scattered light.

The spectrum of the collected scattered light was analyzed by a 0.5 m focal length monochromator with an 1800 line/mm diffraction grating blazed at 500 nm, and detected by a (1340×100) pixel liquid-nitrogen-cooled CCD array photodetector with pixel size of $20 \mu\text{m} \times 20 \mu\text{m}$. The accessible Stokes shift range of our spectrometer was 120 cm^{-1} to $\approx 7000 \text{ cm}^{-1}$. The instrument resolution (defined as the minimum wavenumber difference at which two separate peaks can be distinguished) was $\approx 1 \text{ cm}^{-1}$ in the Stokes shift range of interest for this study. The wavenumber scale was calibrated to an accuracy of $\approx 0.1 \text{ cm}^{-1}$ with spectral lines of Ne and Kr atomic vapor lamps. The reported wavenumber values represent vacuum wavenumber, i.e., $\frac{f}{c}$, where f is the frequency (Hz) and c is the speed of light in vacuum.

Raman spectra of the BC samples were taken from pieces of various sizes, $6 \text{ mm} \times 6 \text{ mm}$ or larger, that were extracted from the original substrates. Because of the large variation of the substrate temperature and NW growth rate with distance from the substrate center in system D, Raman spectra of the D samples were taken from large wedge-shaped pieces that enabled measurement of the distance between the original substrate center and the Raman probed location. All Raman spectra of the D samples were acquired at a distance of $(26.7 \pm 2.0) \text{ mm}$ from the substrate center.

IV. RESULTS

A. Overview of Raman spectra

Raman spectra of samples C024, B982, D262, and D273 are plotted in Fig. 2 to illustrate the observed peaks. The $A_1(TO)$, $E_1(TO)$, and E_2^{high} peaks and the Si substrate peak are shown in Fig. 2(a), which encompasses the 500 cm^{-1} to 600 cm^{-1} range. It can be seen that the frequencies of these modes, indicated by vertical dashed lines, do not vary between samples. From curve-fitting, and then averaging the curve-fitting results for multiple samples, the peak frequencies were found to be $(531.80 \pm 0.02)\text{ cm}^{-1}$ for the $A_1(TO)$ mode, $(558.65 \pm 0.02)\text{ cm}^{-1}$ for $E_1(TO)$, $(567.29 \pm 0.02)\text{ cm}^{-1}$ for E_2^{high} , and $(520.20 \pm 0.02)\text{ cm}^{-1}$ for the Si peak. In addition, the E_2^{low} mode (not shown in Fig. 2) was observed at $\approx 144\text{ cm}^{-1}$. Between 3 and 29 spectra were measured for each of the B/C samples, and 10 spectra were measured for each of the D samples. The curve-fitting procedure is described in the Appendix part 1, and the uncertainty analysis of the fit parameters is described in the Appendix part 2.

The LPP+ and SO peaks for the same samples are shown in Fig. 2(b), which encompasses the 650 cm^{-1} to 830 cm^{-1} range. The LPP+ and SO frequencies and line widths are dependent on carrier concentration and hence vary between samples with different carrier concentrations. The vertical dashed lines in Fig. 2(b) show the fitted LPP+ and SO frequencies for sample C024, which is representative of undoped material with low carrier concentration.

Details of the curve-fitting analysis of a Raman spectrum from sample D262, the same spectrum plotted in Fig. 2, are illustrated in Fig. 3. The data points are shown as small squares, each fitted peak is shown as a dashed line, and the overall fit is shown as a solid line. The difference between the fit and data (residual curve) is plotted below the other curves as a solid line. The fit is seen to be in good agreement with the data. Note the weak peak at 697 cm^{-1} ; this

peak is of unknown origin, but might arise from a local vibrational mode due to defects or impurities. A similar peak was observed in the other D samples.

B. Frequencies of LO, TO, and SO phonon modes

The $A_1(LO)$ and $E_1(LO)$ phonon frequencies, denoted $\nu_{A_1(LO)}$ and $\nu_{E_1(LO)}$, were reported to be 734 cm^{-1} and 741 cm^{-1} , respectively, in a study of single-crystal wurtzite-GaN with low strain and low carrier concentration²². (Note that uncertainty estimates for $\nu_{A_1(LO)}$ and $\nu_{E_1(LO)}$ are not given in Ref. 22.) Frequencies 1 cm^{-1} to 2 cm^{-1} higher were found in other studies^{27, 28}. It will be assumed that Ref. 22 provides the best estimate, and the slightly higher frequencies reported in Refs. 27 and 28 are the result of accidental doping with Si and/or O donor impurities, which is common in GaN growth.

Distinct $A_1(LO)$ and $E_1(LO)$ peaks were not observed in the NW samples. Rather, a single LO phonon or LPP+ peak occurred in each sample. The measured peak frequency ranged from a minimum of $(739.10 \pm 0.02) \text{ cm}^{-1}$, in the nominally undoped sample C024, to a maximum of $(755.73 \pm 0.34) \text{ cm}^{-1}$, in D270. In addition, the peak frequency in the lightly doped sample D299 is $(739.65 \pm 0.05) \text{ cm}^{-1}$. The LO phonon frequency in the undoped sample is seen to lie between the values of $\nu_{A_1(LO)}$ and $\nu_{E_1(LO)}$ given in Ref. 22, but closer to $\nu_{E_1(LO)}$. The reasons for these observations are discussed in the Appendix part 5. The main conclusions of the Appendix part 5 are as follows: the observed LO phonon peak in undoped NWs arises from a mixture of $A_1(LO)$, $E_1(LO)$, and quasi-LO modes, where the frequencies of the quasi-LO modes are intermediate between $\nu_{A_1(LO)}$ and $\nu_{E_1(LO)}$. A mixture of LO phonon modes is observed because the polarization and propagation directions of the incident and scattered light, and hence the phonon propagation directions, are randomized by a diffusive type of light scattering in the

NW ensemble. The observed LO phonon peak in undoped NWs corresponds to a weighted average of the $A_1(LO)$, $E_1(LO)$, and quasi-LO frequencies, as calculated from Eqs. (A25)-(A27).

Substitution of $\nu_{A_1(LO)} = 734.0 \text{ cm}^{-1}$ and $\nu_{E_1(LO)} = 741.0 \text{ cm}^{-1}$ (from Ref. 22) in Eq. (A27) gives the result $\nu_{quasi-LO,avg} = 738.7 \text{ cm}^{-1}$, which is close to the measured peak frequency of $(739.10 \pm 0.02) \text{ cm}^{-1}$ in the undoped sample C024. The latter value assumed to be the best estimate of ν_{LO} for determination of N from Eq. (4). This is equivalent to assuming that $\nu_{LPP+} = \nu_{LO}$ and $N = 0$ in C024. As discussed below, the line shape of the LO phonon / LPP+ line in samples C024 and D299 provides additional support for this assumption.

In contrast to the observation of a single LO phonon / LPP+ peak, distinct $A_1(TO)$ and $E_1(TO)$ peaks were observed in all samples, as illustrated in Fig. 2(a). It can be seen that the $A_1(TO)$ and $E_1(TO)$ line shapes are asymmetric with broadening toward the quasi-TO region; i.e., the $A_1(TO)$ line is broadened on the high-frequency side, and the $E_1(TO)$ line is broadened on the low-frequency side (these asymmetries were confirmed by curve-fitting). In addition, the intensity in the region between $\nu_{A_1(TO)}$ and $\nu_{E_1(TO)}$ is significantly greater than zero. These results support the occurrence of quasi-TO modes between $\nu_{A_1(TO)}$ and $\nu_{E_1(TO)}$.

Substitution of the measured TO phonon frequencies, $\nu_{A_1(TO)} = (531.80 \pm 0.02) \text{ cm}^{-1}$ and $\nu_{E_1(TO)} = (558.65 \pm 0.02) \text{ cm}^{-1}$, in Eq. (A27) gives the result $\nu_{quasi-TO,avg} = (549.79 \pm 0.02) \text{ cm}^{-1}$, which is assumed to be the best estimate of ν_{TO} . The uncertainty estimate for $\nu_{quasi-TO,avg}$ may be too low because there is a possibility of systematic error in the averaging procedure; i.e., the correct weighted average of $\nu_{A_1(TO)}$ and $\nu_{E_1(TO)}$ for determination of N may differ from Eq. (A27). However, increasing the assumed uncertainty of ν_{TO} by a large amount (up to 5 cm^{-1}), to account for this possible systematic error, was found to have a negligible effect on the uncertainty of N .

The measured surface optical (SO) phonon frequency is in good agreement with a simple electrostatic model²⁹, which was derived for zincblende-structure crystals (and hence does not account for the effect of $A_1 - E_1$ splitting). According to the model, the SO phonon frequency can be expressed as

$$\nu_{SO} = \nu_{TO} \left(\frac{\epsilon_s + 1}{\epsilon_\infty + 1} \right)^{1/2} \quad (6)$$

where ν_{TO} is the TO phonon frequency, ϵ_∞ is the high-frequency dielectric constant, and ϵ_s is the static dielectric constant. By substituting the Lydane-Teller-Sachs relation, $\nu_{LO}/\nu_{TO} = (\epsilon_s/\epsilon_\infty)^{1/2}$, into Eq. (6), ν_{SO} can be expressed as a function of ν_{LO} (rather than ν_{TO}):

$$\nu_{SO} = \left(\frac{\epsilon_s + 1}{\epsilon_s} \frac{\epsilon_\infty}{\epsilon_\infty + 1} \right)^{1/2} \nu_{LO} = 0.964 \cdot \nu_{LO} . \quad (7)$$

With substitution of the values $\epsilon_\infty = 5.23$ for the high-frequency dielectric constant, $\epsilon_s = 9.4$ for the static dielectric constant³⁰, and $\nu_{quasi-LO} = 739 \text{ cm}^{-1}$ into Eq. (7), the predicted SO phonon frequency is $\nu_{SO} = 712 \text{ cm}^{-1}$. If, on the other hand, the $A_1(LO)$ phonon frequency of 734 cm^{-1} is substituted into Eq. (7), with the same dielectric constant values, then the predicted SO phonon frequency is $\nu_{SO} = 707 \text{ cm}^{-1}$. The measured SO phonon frequency in sample C024, $(709.50 \pm 0.12) \text{ cm}^{-1}$, is midway between the two predicted values. This comparison suggests that the observed SO mode is a mixed ($A_1 + E_1$) mode, but with a larger admixture of the A_1 component than the observed quasi-LO mode.

C. LPP+ frequencies and carrier concentrations

1. Summary of results

The average LPP+ frequency ($\nu_{LPP+,avg}$) and carrier concentration (N_{avg}) for each sample, and the expanded uncertainties (corresponding to 95 % confidence intervals) $U(\nu_{LPP+,avg})$ and $U(N_{avg})$, are listed in Table II. The parameters $\nu_{LPP+,avg}$ and N_{avg} represent averages over several Raman measurements of each sample, taken from different sample locations or with different polarization geometries. Expressions for $U(\nu_{LPP+,avg})$ and $U(N_{avg})$ are derived in part 2 and part 3 of the Appendix, respectively. The number of measurements of each sample (η) is shown in the last column of Table II. The relationship between N_{avg} and $\nu_{LPP+,avg}$ is plotted in Fig. 4. The function $N(\nu_{LPP+})$ described by Eq. (4) is plotted as a solid line, and each data point shows the average parameter values and uncertainties for a particular sample; the BC samples are indicated by squares, and the D samples are indicated by circles.

The number of measured Raman spectra per sample varies considerably for the BC samples, from $\eta=3$ for C239 to $\eta=27$ for C144 and $\eta=29$ for C024. (The number of spectra is largest for C024 and C144 because additional experiments were done on these samples, as described below.) A more systematic measurement protocol was followed for the D samples. Raman spectra were obtained from five collinear locations in each D sample, with a spacing of 2 mm and thus maximum separation of 8 mm, along a line perpendicular to the substrate radius, at a radial distance (i.e., distance from the center of the substrate) of (26.7 ± 2.0) mm. The distance of 26.7 mm was chosen because electron microscopy (Fig. 1) showed good NW morphology (predominance of NWs with well-defined hexagonal cross-sections, and an absence of coalescence between NWs) and reasonably high density at similar radial distances. The NW morphologies and densities in the D samples are strongly dependent on radial distance.

For each sample, $U(v_{LPP+,avg})$ was calculated by the method described in the Appendix part 2, and $U(N_{avg})$ was calculated from Eq. (A16) in the Appendix part 3. (Although it is assumed that $N_{avg} = 0$ for sample C024, the “nominal” uncertainty of N_{avg} in sample C024 is shown in Table II for comparison to the other samples.)

2. Measurement of inhomogeneous carrier concentration in sample C239

In the BC samples other than C239, the maximum separation between the Raman measurement locations was ≤ 10 mm. In C239, Raman spectra were acquired from six collinear locations denoted #1 to #6, with a spacing of 5 mm and thus maximum separation of 25 mm. Electron microscopy showed a large decrease in NW density from location #1 to location #6. The changes in N (squares) and LPP+ peak intensity (circles) along the measurement line are plotted in Fig. 5. The peak intensity, which is expected to scale with NW density, is seen to decrease by a factor of ≈ 4 from location #1 to location #6, in qualitative agreement with the microscopy results. The carrier concentration, N , decreases by approximately 15 % from location #1 to location #6 and, in addition, the data points fall into two clusters, with higher N at locations #1 to #3 and lower N at locations #4 to #6. (The results for C239 shown in Table II and Fig. 5 include locations #1 to #3 only. This choice was made to better compare the properties of C239 with the other BC samples, because regions of relatively low NW density were not examined in the other samples.)

3. Dependence of carrier concentration on Si cell temperature

N_{avg} is plotted as a function of Si cell temperature (T_{Si}) for the D series specimens in Fig. 6. N_{avg} was found to be 84 % higher in D270 than in D273, although these two samples were

grown with the same Si cell, same T_{Si} , and same or similar values of other growth parameters (see Table I). The unexpectedly high value of N_{avg} in D270 could result from subtle changes in Si incorporation due to changes in the sidewall diffusion of Ga or in the local V:III ratio; the omission of the “expansion step” for D270 (as described in the Experimental Procedure), may also have contributed to the increase in N . The results for the D samples other than D270 are fit very well by an Arrhenius function $N_{\text{avg}}(T_{\text{Si}}) = N_0 e^{-E_a/k_B T}$ with activation energy $E_a = 6.281 \pm 0.011$ eV, which is shown as a dashed line in Fig 6. (Note that, with four data points and two fit parameters, this fit has only two degrees of freedom.)

Si cell temperatures from the BC growth system do not span a sufficient range to allow quantifying the dependence of N_{avg} on T_{Si} . N_{avg} was found to be higher in samples C239, C144, and C236 than in C023 and B982; however, samples C239, C144, and C236 were grown with a different Si cell and 25 °C lower T_{Si} than C023 and B982. This observation shows that changing the cell can have a large effect on the Si flux, because reducing T_{Si} is expected to result in lower N if other growth conditions are unchanged. We have occasionally observed that carrier concentrations are unusually high after work on the N_2 supply lines, as in B738 (which is nominally undoped but shows a significantly higher value of $\nu_{\text{LPP+},\text{avg}}$ than C024), from which we conclude that the supply lines became temporarily contaminated with O_2 or H_2O . Because both O and Si are shallow donors in GaN, either Si incorporation (from the Si cell) or O incorporation (from contaminants) will cause N to increase.

4. Carrier concentration in single-nanowire devices

a. Comparison with electrical measurements

An important application of the Raman measurements is estimation of the carrier concentration in single-NW devices. The Raman-based carrier concentration estimates for samples B982, C023, C144, and C236 (as shown in Table II) are consistent with electrical measurements of devices^{12,18,31,32,33}, including two-terminal devices and transistors, fabricated from these samples. (Note that the Raman measurements of runs B982 and C236 (as summarized in Table II) were obtained from locations on the growth substrate at distances of ≈ 5 mm to 10 mm from the device locations, with the intention of minimizing possible discrepancies in the Raman and electrical measurements due to long-range spatial variation of N . These distances are small compared to the growth substrate diameter of 76.2 mm.)

More specifically, preliminary estimates for the free carrier concentration N derived from our Raman analysis were used in three separate reports of NW transport properties (Refs. 12, 18, and 33) that examined NWs from batches B982 and C236. It should be pointed out that these preliminary values of N were slightly different from the values shown in Table II, due to refinements in methodology during the course of the research, but the differences fall within the uncertainty intervals and hence are not significant. In particular, the preliminary estimates of N given in Ref. 18 for samples B982 and C236 were $(1.2 \pm 0.2) \times 10^{17} \text{ cm}^{-3}$ and $(2.5 \pm 0.3) \times 10^{17} \text{ cm}^{-3}$, respectively. The final estimates of N (from Table II) and the uncertainty of N (from Table III, as discussed below) for single NWs taken from samples B982 and C236 are $(1.08 \pm 0.16) \times 10^{17} \text{ cm}^{-3}$ and $(2.59 \pm 0.30) \times 10^{17} \text{ cm}^{-3}$, respectively. We now briefly review the prior transport studies in order to add more context to the present work.

Parkinson, et al. (Ref. 12) used our preliminary estimate of N for batch B982 as input to their THz photoconductivity measurement of drift mobility μ . They found $\mu = 820 \pm 120$ cm²/(V·s) for dispersed ensembles of NW with mean diameters of 310 nm.

In their study of batch C236, Sanford, et al. (Ref. 18) used the preliminary estimate of N , UV photoconductivity data, and measurements of surface band bending (SBB) as determined by x-ray photoelectron spectroscopy (XPS), to calculate μ for a collection of single-NW devices whose diameters ranged from 75 nm to 194 nm. A conservative error analysis revealed a range of μ from 850 cm²/(V·s) to 2100 cm²/(V·s). Furthermore, they observed no correlation of μ with NW diameter. They reported SBB = 0.2 ± 0.1 eV as determined by XPS.

Henning, et al (Ref. 33) studied the transverse surface photo-voltage (SPV) across hexagonal facets and vertices of NWs from batch C236. With the preliminary Raman-derived value of N as input, 3D finite-element electrostatic analysis returned both the transverse SPV result, and the XPS value for SBB for this wire batch described in Ref. 18.

Hence, the Raman derived estimates of N returned values of drift mobility for wire batches B982 and C236 that were calculated by entirely independent methods and were in agreement within the confines of their respective uncertainties. Moreover, in batch C236, the assumption that the same Raman-derived value of N is applicable for a collection of uniform single- NW devices ranging in diameter from 75 nm to 194 nm is not contradicted within the estimated uncertainty for the combined UV photoconductivity and XPS analysis. Finally, for batch C236, self-consistent results for SPV and XPS-derived SBB are found when the Raman-derived value of N is used as input for a fully 3D finite-element Poisson electrostatic analysis.

b. Uncertainty estimation

If the variation of N within the set of η measurements of a given sample arises primarily from inhomogeneity (e.g., spatial variation within the region of interest that contains the Raman measurement locations and NW device locations), then the appropriate uncertainty estimate for N in a single NW is larger than the uncertainty estimate for N_{avg} which is shown in Table II.

The reason for the increased uncertainty estimate is that taking one NW from an arbitrary location within the region of interest can be considered as equivalent to randomly selecting one value of N from an inhomogeneous distribution of values of N . The interval that contains one randomly selected value of N with 95 % probability, denoted $[N_{avg} \pm W(N_{avg})]$, is larger than the interval that contains the mean value of N with 95 % probability, denoted $[N_{avg} \pm U(N_{avg})]$; i.e., $W(N_{avg}) > U(N_{avg})$, where $U(N_{avg})$ is shown in Table II. Expressions for $U(N_{avg})$ (Eqs. (A16) and (A17)) and $W(N_{avg})$ (Eq. (A18)) are derived in the Appendix part 3. The calculated values of $W(N_{avg})$ are listed in Table III.

Further, according to the discussion in the Appendix part 3, $W(N_{avg})$ can be expressed as a quadrature sum of three components, denoted U_{mater} , W_{intra} , and $W_{inhomog}$, which are listed in columns 3 to 5 of Table III. The first component, U_{mater} (Eq. (A16b)), arises from the uncertainties of the material properties parameters (m^* , ϵ_∞ , ν_{LO} , ν_{TO}). These parameters are assumed to be fixed; thus, the variation of N between measurements is entirely determined by the variation of ν_{LPP+} . The second and third components, W_{intra} (Eqs. (A16c) and (A18)) and $W_{inhomog}$ (Eqs. (A17b) and (A18)), arise from the uncertainty of ν_{LPP+} . W_{intra} corresponds to the “intra-spectral” component of the uncertainty of ν_{LPP+} , which is due to instrumental factors such as noise in the Raman data and wavenumber calibration drift. $W_{inhomog}$ corresponds to the

component of the uncertainty of ν_{LPP+} that arises from inhomogeneous broadening (e.g., spatial variation of the material properties). From Table III, $W_{inhomog}$ is seen to be the dominant component of $W(N_{avg})$ in most samples. Also, $W(N_{avg})$ is significantly larger in the samples with $N_{avg} > 10^{17} \text{ cm}^{-3}$ than in the undoped sample C024 and the low-doped sample D299.

c. Raman measurements of single nanowires

While in principle, Raman measurements of a single NW in a device could enable determination of N with lower uncertainty than the method discussed here, we found that our instrumentation lacked sufficient sensitivity to observe the LO or LPP+ peak, and hence quantify ν_{LPP+} , in dispersed single NWs. The lack of sensitivity for dispersed single NWs is driven by several factors. Firstly, the Raman excitation volume is smaller for a single NW than for an ensemble. Assume that the micrographs of sample D273 in Fig. 1 represent typical NW dimensions and ensemble morphology. A typical NW is then estimated to have a diameter of 200 nm and length of 12 μm , and the areal number density of NWs in the ensemble is $\approx 6 \mu\text{m}^{-2}$. The excitation volume for an elliptical $2.4 \mu\text{m} \times 1.0 \mu\text{m}$ laser spot intersecting one NW is then $0.031 \mu\text{m}^3$ to $0.075 \mu\text{m}^3$ (depending on orientation of the major axis of the ellipse relative to the NW axis), while the excitation volume for the same laser spot intercepting an as-grown ensemble of NWs is at least $4.3 \mu\text{m}^3$. The excitation volume for the as-grown ensemble is further enhanced by diffusive light scattering, as discussed in the Appendix part 5, which increases the effective spot size for the laser-sample interaction.

Secondly, an experiment geometry based on backscatter from dispersed NWs lying flat on a substrate is unfavorable for observation of LO or LPP+ modes. According to the Raman selection rules listed in Table 2 of Ref. 41, the $A_1(LO)$ mode is allowed only for the $z(yy)\bar{z}$

geometry (with the notation introduced in the Appendix part 5), and the $E_1(LO)$ mode is allowed only for $x(yz)y$. The $z(yy)\bar{z}$ geometry requires aligning the incident and scattered propagation directions with the NW axis, which is difficult to attain for a dispersed NW lying flat on a substrate, while the $x(yz)y$ geometry requires right-angle scattering.

Thirdly, the absolute Raman scattering cross-sections of the LO, quasi-LO, and LPP modes in (wurtzite structure) GaN are small compared to the Raman scattering cross-sections of optical phonon modes in other III-V materials such as GaAs. In particular, from Ref. 34, the Raman cross-section of the TO phonon mode in undoped GaAs is calculated to be $1.3 \times 10^{-3} \text{ m}^{-1} \text{ sr}^{-1}$ at $\approx 514 \text{ nm}$ excitation wavelength. From Ref. 35, the Raman cross-section of the E_2^{high} mode in GaN was measured to be $3.8 \times 10^{-5} \text{ m}^{-1} \text{ sr}^{-1}$ at 514 nm , or a factor of 34 smaller than the TO mode in undoped GaAs, and the other first-order Raman modes in GaN had even smaller cross-sections. In addition, for the sample type and experiment geometry used in this study, the measured LPP+ to E_2^{high} peak intensity ratio was low and decreased with increasing N ; this intensity ratio ranged from 0.122 ± 0.006 for undoped material (sample C024) to 0.050 ± 0.005 for $N \approx 3 \times 10^{17} \text{ cm}^{-3}$ (D273). Because of the relatively large Raman cross-sections of the optical phonon modes in GaAs, it is not surprising that Raman measurements of single GaAs NWs have been successful; for example, LPP modes of single p-type GaAs NWs were measured with good-signal-to-noise by transmission Raman spectroscopy, as shown in Fig. 4 of Ref. 14.

A few reports in the literature show the promise of Raman carrier concentration measurements of single GaN NWs, in spite of the difficulty of such measurements. Resonant Raman spectroscopy, with excitation wavelength near the direct band gap of a semiconductor ($\approx 364 \text{ nm}$ for GaN), is an established method for attaining large Raman cross-sections. In a resonant Raman study¹⁶ of single core-shell GaN/AlN NWs with excitation wavelength of 351

nm and power of 1 mW, a strong quasi-LO peak was observed in the $z(y-\bar{z})$ geometry (i.e., with polarization of the scattered light not analyzed). Also, in a Raman study of single GaN NWs of varying diameter³⁶ from 60 nm to 220 nm, with excitation wavelength of 532 nm, laser power of 14 mW, spot diameter of 500 nm, and focusing objective numerical aperture of 0.9, a well-defined, narrow $E_1(LO)$ peak at 743 cm^{-1} was observed with the nominal $x(yz)\bar{x}$ scattering geometry for the largest diameter (220 nm) NW (see the inset to Fig. 4 of Ref. 36). Although the $E_1(LO)$ mode is forbidden for $x(yz)\bar{x}$, the experimental conditions of Ref. 36, in particular the large numerical aperture which produces a mixture of propagation directions, may have induced an admixture of the $x(yz)y$ geometry, for which $E_1(LO)$ is allowed. Carrier concentration effects on the Raman spectrum were not examined in Refs. 16 and 36 (in Ref. 16, the GaN part of the core/shell structure was Si-doped with a high estimated carrier concentration of $2 \times 10^{19}\text{ cm}^{-3}$, but the effect of varying the doping density was not investigated; in Ref. 36, the NWs were undoped). However, results of these studies suggest that Raman carrier concentration measurements of single doped NWs are feasible with similar experimental conditions. Such measurements are a promising topic for future work.

D. Carrier concentration dependence of selected Raman line shape parameters

Several parameters determined by curve-fitting are listed in Table IV: the full width at half maximum (FWHM) of the LPP+ line ($w_{0,LPP+}$), the width asymmetry of the LPP+ peak as defined by Eq. (A3b)) ($w_{A,LPP+}$), the peak frequency of the SO line (ν_{SO}), and the peak frequency of a line at $\approx 696\text{ cm}^{-1}$ (ν_{LVM}). (Note that the listed parameter values represent averages over η measurements of each sample, as discussed above for ν_{LPP+} and N ; in this section, the “avg”

subscript is omitted for conciseness.) The $\approx 696 \text{ cm}^{-1}$ line is tentatively ascribed to a defect-related local vibrational mode, and was observed in only 5 samples.

The dependences of $w_{0,LPP+}$ and $w_{A,LPP+}$ on N are plotted in Figs. 7(a) and 7(b), respectively. (Note that sample C236 is omitted from Figs. 7(a) and 7(b) because of the large uncertainties of the line shape parameters in this sample.) The FWHM of the LPP+ peak is seen to increase with N . This line broadening is ascribed to the effect of plasmon damping on the LPP+ mode, which increases in strength as the mode becomes more plasmon-like in character with increasing carrier concentration.³ The width asymmetry parameter $w_{A,LPP+}$ shows a more complicated dependence on N . $w_{A,LPP+}$ is slightly negative in the undoped (C024) and low-doped (D299) samples, becomes positive and reaches a maximum value at $N \approx 2 \times 10^{17} \text{ cm}^{-3}$, and then decreases with further increases in N and becomes negative again in the highest- N sample (D270). The mechanism for the non-monotonic dependence of the width asymmetry on N is not known.

The measured values of $w_{0,LPP+}$ and $w_{A,LPP+}$ in the lowest- N samples (C024 and D299) provide confirmation of the quasi-LO phonon averaging model for ν_{LO} (Eqs. (A25)-(A27) and surrounding discussion). If the model is correct, then the distribution of quasi-LO phonon frequencies should contribute to the LO phonon line shape. The width of this distribution is $\nu_{E_1(LO)} - \nu_{A_1(LO)} \approx 7 \text{ cm}^{-1}$, and the width asymmetry is estimated to be $(\nu_{E_1(LO)} - \nu_{quasi-LO,avg}) - (\nu_{quasi-LO,avg} - \nu_{A_1(LO)}) \approx -\frac{1}{3}(\nu_{E_1(LO)} - \nu_{A_1(LO)}) \approx -2.3 \text{ cm}^{-1}$. It is likely that the observed LO phonon line shape arises from the convolution of the quasi-LO frequency distribution with a symmetric Lorentzian (phonon lifetime broadening) component; in this case, the linewidth should increase and the magnitude of the asymmetry should decrease from the estimates based solely on the quasi-LO frequency distribution. In other words, the model

prediction is that $w_{0,LPP+} \gtrsim 7 \text{ cm}^{-1}$ and $w_{A,LPP+} \gtrsim -2.3 \text{ cm}^{-1}$ for the convolved line shape.

The experimental results for sample C024, $w_{0,LPP+} = (9.25 \pm 0.08) \text{ cm}^{-1}$ and $w_{A,LPP+} = (-1.61 \pm 0.06) \text{ cm}^{-1}$, and the similar results for D299, are consistent with this prediction.

The dependence of ν_{SO} on N is plotted in Fig. 7(c), and the correlation of ν_{SO} with $\nu_{LPP+,avg}$ is plotted in Fig. 7(d). In Fig. 7(c), ν_{SO} is seen to increase with increasing N . The dashed line in Fig. 7(d) is a linear fit which is constrained to pass through the data point for C024, and excludes the two highest- N samples (D273 and D270). The slope of the line is 0.98 ± 0.24 , and the coefficient of correlation is 0.916. On the other hand, if the highest- N samples are included in the fit, then the slope changes to 0.68 ± 0.18 , and the coefficient of correlation decreases to 0.880 (the latter fit is not shown in Fig. 7(d)).

The observation that there is a 1:1 correlation between the shifts of ν_{SO} and ν_{LPP+} with N (i.e., the slope of this correlation is indistinguishable from unity) for the samples with $N < 3 \times 10^{17} \text{ cm}^{-3}$ is interesting. This observation implies that, within some range of carrier concentration, the SO phonon frequency is dependent on carrier concentration via the same phonon-plasmon coupling mechanism as the LPP+ frequency.

E. Surface depletion effects and UV co-illumination experiment

In a Raman measurement of a NW ensemble, the carrier concentration cannot be assumed to be homogeneous throughout the probed volume. Several effects may contribute to an inhomogeneous distribution of carriers, thus complicating the interpretation of the results. One potentially important source of inhomogeneity is carrier depletion due to band-bending near the surface of a NW. Electronic and optoelectronic measurements of single NW devices, taken from growth runs examined in this study, have revealed significant surface depletion effects¹⁸.

Because the wire diameter varies within an ensemble, the magnitude of the surface depletion effect will vary between wires. The smallest-diameter wires in a given ensemble may be fully depleted, while only a small fraction of the total volume may be depleted for the largest-diameter wires. (It was also suggested in an earlier study⁶ that surface depletion may affect the Raman spectrum of an ensemble of NWs with varying diameters.)

To test the hypothesis that the Raman results are affected by surface depletion, measurements of several samples (B738, C023, B982, and C144) were done under co-illumination by a UV laser with a photon energy of 3.81 eV (wavelength of 325 nm), which exceeds the GaN band gap of 3.4 eV. The UV excitation intensity at the sample was either 0.7 W/cm² or 4.5 W/cm², and the spot size was 250 μm \times 460 μm . Although the UV intensity could have been increased further by reducing the spot size, excitation intensity above 4.5 W/cm² was not used because the UV illumination produced a strong fluorescence background in the Raman spectral region, which increased with excitation intensity. This fluorescence background raised the “noise floor” of the Raman spectrum, and thus increased the uncertainty of the carrier concentration measurements.

Previous studies^{18,31,37} have shown that above-band-gap illumination in this intensity range substantially reduces or eliminates surface depletion in GaN NWs. More specifically, according to the model presented in Ref. 18, the main effect of the above-band-gap UV illumination is to fill in surface states and flatten the bands near the surface (where there is band-bending and at least partial carrier depletion in the absence of above-band-gap excitation). Thus, the carrier concentration near the surface of the NW will increase significantly under UV excitation, while the carrier concentration in the bulk of the NW will be essentially unchanged.

Results of the UV co-illumination experiment are shown in Table V. (A preliminary version of these results was presented in Ref. 18.) The LPP+ and SO peak frequencies, and the calculated carrier concentrations, were found to increase with UV illumination in all cases. The uncertainties of $\Delta\nu_{LPP+}$, $\Delta\nu_{SO}$, and ΔN are seen to be larger for the higher UV intensity. This increase in measurement uncertainty is ascribed to the “noise floor” due to the UV-induced fluorescence background, which increases with excitation intensity, as mentioned above. We thus consider the results of the lower UV intensity (0.7 W/cm^2) measurements to be more meaningful. From the last column of Table V, it can be seen that the fractional increase of the carrier concentration with UV illumination is small for all samples examined in this experiment. Even for sample B738, which showed the largest ΔN and smallest N_{avg} (in the absence of UV), the ratio $\Delta N/N_{avg}$ is only 0.12 ± 0.09 . For sample B982, which was a source of single NW devices for transport measurements, $\Delta N/N_{avg}$ is negligible (0.010 ± 0.021).

The value of $\Delta\nu_{SO}$ at the lower UV intensity is larger than the corresponding value of $\Delta\nu_{LPP+}$ in each sample, by a factor between 3 and 26. Because the SO mode is localized near the surface, it is reasonable to assume that the SO mode is more sensitive to the near-surface carrier concentration than the LPP+ mode. Thus, it is not surprising that the UV excitation has a much larger effect on ν_{SO} than $\Delta\nu_{LPP+}$.

It may be asked why the surface depletion effect on the Raman measurements of carrier concentration is so small. One possibility is that the Raman signal arises primarily from the larger-diameter NWs in each measurement, in which the volume fraction occupied by the depletion layer is small. Another possibility is that the depletion is substantially reduced from true dark conditions in the Raman experiments, even without UV co-illumination, due to photo-excitation by the intense (65 kW/cm^2 to 370 kW/cm^2), below-band-gap (1.96 eV) Raman laser.

The latter hypothesis has strong support from the observation (see Fig. 10 of Ref. 18) that below-gap (2.25 eV) illumination with intensity as low as 0.2 mW/cm² (nine orders of magnitude below the typical Raman excitation intensity) induces observable photoconductivity in single NWs.

F. Effect of material with non-nanowire morphology

Some growth runs from the BC system contain a significant amount of GaN material with a faceted, non-NW morphology, in a continuous layer near the substrate. (Of the D samples, only sample D262 contains an observable matrix layer, and this layer is thinner than the matrix layers in several BC samples.) The layer of faceted, non-NW material is referred to as the “matrix layer” in previous reports.^{23,38} A matrix layer with thickness of approximately 8 μm is seen in the cross-sectional view of sample B982 (Fig. 1). If the carrier concentration is different in the matrix layer than in the NWs, the matrix layer contribution to the Raman spectrum can lead to a difference between the Raman carrier concentration and the carrier concentration obtained from electrical measurements of single NWs. An experiment was performed to assess the significance of this effect, as follows.

NWs were removed from a small sample region, leaving the more strongly adherent matrix layer intact, by scraping with a wetted cotton swab. Then a Raman spectrum was measured in the scraped region, and another spectrum was measured in an adjacent as-grown (not scraped) region. A weighted difference between the second spectrum (“as-grown: NWs + matrix”) and the first spectrum (“scraped: matrix layer only”) was calculated, with the weighting chosen to null out the narrow Si substrate peak, which is present in both spectra. It is assumed that the contribution of the matrix layer as well as the Si substrate is nulled out when the weighted difference is calculated; thus the “difference” spectrum shows the contribution of the

NWs only, with the contributions of the matrix layer and substrate removed. In the final step, curve-fitting was used to determine changes in LPP+ frequencies and carrier concentrations on going from the “as-grown” to the “difference” spectrum.

Examples of “as-grown: NWs + matrix”, “scraped: matrix only”, and “difference: NWs only” spectra from runs B738 and B982 are shown in Figs. 8(a) and 8(b), respectively. Note the derivative-like feature at $\approx 520 \text{ cm}^{-1}$ in the difference spectrum of B738 (lower curve, Fig. 8(a)). The derivative-like feature indicates imperfect nulling of the Si substrate peak, due to a shift of the Si peak frequency between the as-grown and scraped spectra. (The Si peak shift between the as-grown and scraped regions probably arises from spatially varying stresses in the near-surface region of the Si substrate; the Si Raman frequency is sensitive to stress state.)

Table VI shows the curve-fitting results from four measurements of B738 and six measurements of B982. The parameters listed are the change in LPP+ frequency from the “as-grown: NWs + matrix” spectrum to the corresponding “difference: NWs only” spectrum, denoted $\Delta\nu_{LPP+}$, and the calculated change in carrier concentration, denoted ΔN . (Note that the results shown in Table II for samples B738 and B982 are derived from the “difference: NWs only” spectra from this experiment.)

From Table VI, the average value and uncertainty of ΔN for run B982, averaged over six measurements, is $(-8.8 \pm 3.8) \times 10^{15} \text{ cm}^{-3}$; i.e., the decrease in N from the “as-grown” to the “difference” spectra is significantly different than zero. If the scraping experiment had not been performed, then the matrix layer contribution to the “as-grown” spectra from B982 would cause the carrier concentration in the NWs to be overestimated by $\approx 9 \times 10^{15} \text{ cm}^{-3}$, or $\approx 8 \%$ of the total carrier concentration. On the other hand, the average value and uncertainty of ΔN for run B738, averaged over four measurements, is $(-1.2 \pm 3.9) \times 10^{15} \text{ cm}^{-3}$, well below the level of statistical

significance. It appears that, because of the large FWHM of the LPP+ peak in matrix layer material as compared to NW material in B738 (Fig. 8(b)), the matrix layer has a negligible effect on the measurement of ν_{LPP+} and hence the determination of N in this sample.

G. Test of surface-plasmon or bulk-plasmon character of LPP+ mode

1. Model and experiment design

Thus far, we have assumed that the relationship between the carrier concentration (N) and plasmon frequency (ν_p) is given by Eq. (2), which describes bulk plasmon modes. This assumption was also made in previous Raman studies of GaN NWs.^{4,5} However, it appears plausible that, due to the small dimensions of the NWs, the plasmon component of the LPP+ mode in a NW may be described as a surface plasmon (SP) rather than bulk plasmon (BP) excitation. For a surface plasmon, the electromagnetic fields are localized at the conductor-dielectric (e.g., NW-air) interface. The dependence of the SP frequency (ν_{SP}) on N for a cylindrical (or planar) conductor³⁹ in a medium of high-frequency dielectric constant ϵ_{med} is

$$\nu_{SP}(N) = \left(\frac{1}{2\pi c}\right) \left(\frac{Ne^2}{(\epsilon_{med} + 1)m^*m_e\epsilon_\infty\epsilon_0}\right)^{1/2} = (\epsilon_{med} + 1)^{-1/2} \left(\frac{N}{K m^*\epsilon_\infty}\right)^{1/2} \quad (8)$$

(where K is defined by Eq. (3)). Comparison of Eqs. (2) and (8) shows that, for a given value of N , $\nu_{SP}(N)$ is smaller than the BP frequency, $\nu_{BP}(N)$, by a factor of $(\epsilon_{med} + 1)^{-1/2}$ or, equivalently, the ratio $N/\nu_{SP}^2(N)$ is larger than $N/\nu_{BP}^2(N)$ by a factor of $(\epsilon_{med} + 1)$. In other words, if the BP model (Eq. (2)) is used to calculate N , but the SP model (Eq. (8)) is correct, then the actual value of N will be a factor of $(\epsilon_{med} + 1)$ larger than the calculated value, where $(\epsilon_{med} + 1) = 2$ in air. To have confidence that the calculated values of N are accurate, it is necessary to determine whether the BP (Eq. (2)) or SP (Eq. (8)) model is correct.

A Raman-based experimental test was performed to resolve this issue. The concept of the experiment is immersion of an n-type doped NW sample in a transparent oil with a high dielectric constant compared to air ($\epsilon_{oil} > \epsilon_{air} = 1$), and comparison of Raman spectra acquired before and after oil immersion. The sample chosen for the experiment was C144, and the oil used was Cargille Labs type LDF (very low fluorescence) microscope immersion oil²⁶. From manufacturer-provided data on refractive index dispersion in the visible region, the refractive index of the oil at the Raman excitation (633 nm) or scattering (≈ 664 nm) wavelength is $n_{oil} = 1.51$, and the high-frequency dielectric constant is $\epsilon_{oil} = 2.24$. (The value of ϵ_{oil} was determined from a Sellmeier fit to the refractive index dispersion data, analogous to Eq. (A22) in the Appendix part 4.) From Eqs. (2) and (8), the oil immersion is predicted to reduce ν_{SP} by a factor of $\left(\frac{\epsilon_{air} + 1}{\epsilon_{oil} + 1}\right)^{1/2} = 0.786$ relative to air, and to have no effect on ν_{BP} .

Interpretation of the experimental results would be straightforward if the plasmon frequency (ν_{BP} or ν_{SP}) were measured directly. However, the coupled phonon-plasmon frequency measured in the Raman experiments, ν_{LPP+} , is a function of the LO and TO phonon frequencies as well as the plasmon frequency. As explained in section IV.B and the Appendix part 5, the value of ν_{LO} (or ν_{TO}) in Eq. (1) and Eq. (4) is a weighted average frequency (see Eq. (A27)) corresponding to a mixture of LO and quasi-LO phonon modes (or TO and quasi-TO phonon modes). The mechanism for the mixing of the phonon modes is diffusive, elastic light scattering that causes randomization of the optical polarization and propagation directions, and hence the phonon propagation direction, within the ensemble of NWs probed in the experiment. The diffusive light scattering arises from the refractive index mismatch between the NWs and the surrounding medium (air or oil). Oil immersion will reduce the refractive index mismatch between the NWs and the surrounding medium; i.e., $n_{NW} - n_{oil} < n_{NW} - n_{air}$ (where n_{NW} and

n_{air} are, respectively, the refractive indices of the NWs and air). In addition, oil immersion will reduce the angle of incidence of the laser beam on the sample surface from 65° (the angle of incidence in air) to 37° , due to refraction at the air-oil interface, before the laser beam reaches the NWs. Both the reduction of the refractive index mismatch and the reduction of the angle of incidence, due to the oil immersion, will modify the diffusive light scattering process and hence cause the effective optical phonon frequencies, ν_{LO} and ν_{TO} , to be different in oil than in air.

The following equations, which take into account the effect of oil immersion on ν_{SP} , ν_{LO} , and ν_{TO} , were used to analyze the experimental results. If the SP model (Eqs. (8) and (4)) is correct, then, from Eq. (8) (noting that the NW material properties N , m^* , and ϵ_∞ are not modified by oil immersion),

$$\frac{N}{K m^* \epsilon_\infty} = (\epsilon_{oil} + 1)(\nu_{SP,oil})^2 = (\epsilon_{air} + 1)(\nu_{SP,air})^2, \quad (9a)$$

and hence, from Eq. (4),

$$\frac{\nu_{L+,oil(SP)}^2(\nu_{L+,oil(SP)}^2 - \nu_{LO,oil}^2)}{(\nu_{L+,oil(SP)}^2 - \nu_{TO,oil}^2)} = \left(\frac{\epsilon_{air} + 1}{\epsilon_{oil} + 1} \right) \frac{\nu_{L+,air}^2(\nu_{L+,air}^2 - \nu_{LO,air}^2)}{(\nu_{L+,air}^2 - \nu_{TO,air}^2)}, \quad (9b)$$

where $\nu_{SP,air}$, $\nu_{LO,air}$, and $\nu_{TO,air}$ are the SP, LO phonon, and TO phonon frequencies in air;

$\nu_{SP,oil}$, $\nu_{LO,oil}$, and $\nu_{TO,oil}$ are the corresponding frequencies in oil; $\nu_{L+,air}$ is the measured LPP+

frequency in air; $\nu_{L+,oil(SP)}$ is the LPP+ frequency in oil predicted by the SP model; and

$\left(\frac{\epsilon_{air} + 1}{\epsilon_{oil} + 1} \right) = 0.617$. On the other hand, if the BP model (Eqs. (2) and (4)) is correct, then

$\nu_{BP,oil} = \nu_{BP,air}$ and hence

$$\frac{\nu_{L+,oil(BP)}^2(\nu_{L+,oil(BP)}^2 - \nu_{LO,oil}^2)}{(\nu_{L+,oil(BP)}^2 - \nu_{TO,oil}^2)} = \frac{\nu_{L+,air}^2(\nu_{L+,air}^2 - \nu_{LO,air}^2)}{(\nu_{L+,air}^2 - \nu_{TO,air}^2)}. \quad (10)$$

where $\nu_{L+,oil(BP)}$ is the LPP+ frequency in oil predicted by the BP model. The LPP+ frequencies in oil predicted by the SP and BP models, $\nu_{L+,oil(SP)}$ and $\nu_{L+,oil(BP)}$ respectively, can then be compared with the measured LPP+ frequency in oil, denoted $\nu_{L+,oil(meas)}$.

Approximate expressions for $\nu_{L+,oil(SP)}$ and $\nu_{L+,oil(BP)}$, which provide a more intuitive understanding of the effect of oil immersion, can be derived from the linearized approximation to Eq. (4) given by Eqs. (5a) and (5b), with the further approximation

$$\frac{2\nu_{LO,oil}^3}{(\nu_{LO,oil}^2 - \nu_{TO,oil}^2)} \approx \frac{2\nu_{LO,air}^3}{(\nu_{LO,air}^2 - \nu_{TO,air}^2)} . \quad (11)$$

From Eqs. (5a), (5b), (8), and (11),

$$\nu_{L+,oil(SP)} \approx \nu_{LO,oil} + \left(\frac{\epsilon_{air} + 1}{\epsilon_{oil} + 1} \right) (\nu_{L+,air} - \nu_{LO,air}) \quad (12a)$$

or, equivalently,

$$\nu_{L+,oil(SP)} \approx \nu_{L+,air} + (\nu_{LO,oil} - \nu_{LO,air}) - \left(\frac{\epsilon_{oil} - \epsilon_{air}}{\epsilon_{oil} + 1} \right) (\nu_{L+,air} - \nu_{LO,air}) . \quad (12b)$$

From Eqs. (5a), (5b), (2), and (11),

$$\nu_{L+,oil(BP)} \approx \nu_{L+,air} + (\nu_{LO,oil} - \nu_{LO,air}) . \quad (13)$$

According to these approximations, both $\nu_{L+,oil(SP)}$ and $\nu_{L+,oil(BP)}$ are shifted from the LPP+ frequency in air ($\nu_{L+,air}$) by the amount $(\nu_{LO,oil} - \nu_{LO,air})$; this shift arises from the effect of oil immersion on the diffusive light scattering within the NW ensemble. In addition, $\nu_{L+,oil(SP)}$ is down-shifted from $\nu_{L+,oil(BP)}$ by an amount proportional to $(\nu_{L+,air} - \nu_{LO,air})$; this shift arises from the effect of oil immersion on the SP frequency. Note that the calculations discussed below utilize Eqs. (9b) and (10), rather than the approximate forms given by Eqs. (12b) and (13).

2. Results

A typical Raman spectrum of sample C144 in oil is displayed in Fig. 9(a). A number of peaks occur in the 630 cm^{-1} to 830 cm^{-1} range; most of these peaks are attributed to molecular vibrations of the immersion oil constituents. The oil-derived peaks were removed by measuring the spectrum of the immersion oil on a bare Si substrate (the bottom spectrum in Fig. 9(a)), and then calculating a weighted difference of the “C144 in oil” spectrum and the “oil only” spectrum (the top spectrum in Fig. 9(a)). Typical Raman spectra of C024 in air, C024 in oil, C144 in air, and C144 in oil are plotted in Fig. 9(b).

From Raman measurements of nine locations on sample C144, arranged in a square grid with side length of 4 mm, the average LPP+ frequencies in air and oil, $\nu_{L+,air}$ and $\nu_{L+,oil(meas)}$, were found to be $(744.44 \pm 0.21) \text{ cm}^{-1}$ and $(743.69 \pm 0.27) \text{ cm}^{-1}$, respectively. The locations measured in oil differed from the corresponding locations in air, due to refraction of the incident laser beam at the air-oil interface and subsequent defocusing in the oil. (Note that the frequency $\nu_{L+,air}$ measured in the oil immersion experiment differs slightly from the frequency $\nu_{LPP+,avg}$ for sample C144 listed in Table II, which is $(744.58 \pm 0.16) \text{ cm}^{-1}$. The reason for this discrepancy is that $\nu_{LPP+,avg}$ in Table II represents an average over a larger set of locations than the locations examined in the oil immersion experiment.)

The additional parameters needed to calculate $\nu_{L+,oil(SP)}$ and $\nu_{L+,oil(BP)}$ from Eqs. (9b) and (10) were determined as follows. As discussed previously, from measurements of sample C024 (which is assumed to be representative of undoped material), the effective LO and TO frequencies in air were found to be $\nu_{LO,air} = (739.10 \pm 0.02) \text{ cm}^{-1}$ and $\nu_{TO,air} = (549.79 \pm 0.02) \text{ cm}^{-1}$. From measurements in oil of five locations on sample C024, the average LO phonon frequency in oil was found to be $\nu_{LO,oil} = (737.17 \pm 0.17) \text{ cm}^{-1}$. The average TO

phonon frequency in oil was estimated by assuming that the ratio of $(\nu_{TO,oil} - \nu_{TO,air})$ to the full TO frequency range, $\nu_{E_1(TO)} - \nu_{A_1(TO)}$, is the same as the ratio of $(\nu_{LO,oil} - \nu_{LO,air})$ to the full LO frequency range, $\nu_{E_1(LO)} - \nu_{A_1(LO)}$:

$$\nu_{TO,oil} = \nu_{TO,air} + \frac{\nu_{E_1(TO)} - \nu_{A_1(TO)}}{\nu_{E_1(LO)} - \nu_{A_1(LO)}} (\nu_{LO,oil} - \nu_{LO,air}) = (542.39 \pm 0.65) \text{ cm}^{-1} . \quad (14)$$

With these input values, the prediction of the SP model for the LPP+ frequency in oil is $\nu_{L+,oil(SP)} = (740.54 \pm 0.22) \text{ cm}^{-1}$, and the prediction of the BP model is $\nu_{L+,oil(BP)} = (742.67 \pm 0.28) \text{ cm}^{-1}$. Both of the model predictions are below the measured LPP+ frequency in oil of $(743.69 \pm 0.27) \text{ cm}^{-1}$. The experimental result calls into question the assumption (included in both models) that the component of the LPP+ frequency shift due to the oil immersion effect on light scattering is the same as the LO phonon frequency shift; this assumption corresponds to the term $(\nu_{LO,oil} - \nu_{LO,air})$ in the approximate expressions for $\nu_{L+,oil(SP)}$ (Eq. 12(b)) and $\nu_{L+,oil(BP)}$ (Eq. (13)). Nevertheless, the quantitative discrepancy between the SP model for the LPP+ frequency in oil and the experimental result, $\nu_{L+,oil(SP)} - \nu_{L+,oil(meas)} = (-3.15 \pm 0.35) \text{ cm}^{-1}$, is much larger than the discrepancy between the BP model and the experimental result, $\nu_{L+,oil(BP)} - \nu_{L+,oil(meas)} = (-1.02 \pm 0.39) \text{ cm}^{-1}$. We thus conclude that the large downshift of the LPP+ frequency predicted by the SP model is inconsistent with the experimental result, and the BP model for the plasmon component of the LPP+ mode (Eq. (2)) is correct.

From Fig. 9(b), oil immersion is seen to produce a significant downshift of the surface optical (SO) phonon peak (the lower-frequency peak in each spectrum). This effect is simply explained by the increase in dielectric constant of the surrounding medium from air ($\epsilon_{air} = 1$) to

oil ($\epsilon_{oil} = 2.24$). According to Eq. (6) or Eq. (7) for the SO phonon frequency, the frequency change from air to oil is predicted to be

$$\nu_{SO}(\text{oil}) = \left(\frac{\epsilon_s + \epsilon_{oil}}{\epsilon_s + \epsilon_{air}} \frac{\epsilon_{\infty} + \epsilon_{air}}{\epsilon_{\infty} + \epsilon_{oil}} \right)^{1/2} \nu_{SO}(\text{air}) . \quad (15)$$

From the measurements of five locations on C024, $\nu_{SO}(\text{air}) = (709.35 \pm 0.14) \text{ cm}^{-1}$; hence the predicted value of $\nu_{SO}(\text{oil})$ from Eq. (15) is $(685.34 \pm 0.14) \text{ cm}^{-1}$, which is close to the measured value of $(686.04 \pm 0.17) \text{ cm}^{-1}$. From the measurements of nine locations on sample C144, $\nu_{SO}(\text{air}) = (715.45 \pm 0.16) \text{ cm}^{-1}$; hence the predicted value of $\nu_{SO}(\text{oil})$ is $(691.23 \pm 0.15) \text{ cm}^{-1}$, which matches the measured value of $(691.17 \pm 0.36) \text{ cm}^{-1}$.

V. CONCLUSIONS

Modeling of the frequency of the longitudinal phonon – plasmon (LPP+) mode, as observed by Raman spectroscopy, was shown to be a useful technique for estimating the carrier concentration in n-type GaN NW samples. The Raman-measured carrier concentrations in the Si-doped NW samples examined in this study ranged from $(5.28 \pm 1.19) \times 10^{16} \text{ cm}^{-3}$ to $(6.16 \pm 0.35) \times 10^{17} \text{ cm}^{-3}$. Co-illumination by an above band gap UV laser (325 nm, excitation intensity = 0.7 W/cm^2) induced small increases in carrier concentration in the samples in which this effect was investigated. The lowest Si-doped sample showed the largest increase in carrier concentration with UV co-illumination, $(6.3 \pm 4.8) \times 10^{15} \text{ cm}^{-3}$. These results imply that surface depletion does not have a significant effect on the Raman carrier concentration measurements. Immersion in a high-dielectric-constant oil ($\epsilon=2.24$) caused downshifts of similar magnitude in the LPP+ frequencies of undoped and doped NWs, which implies that the LPP+ mode has bulk plasmon rather than surface plasmon character. A surface optical (SO) phonon peak was

observed in each NW sample at a frequency of $\approx 96.4\%$ of the LPP+ frequency, as predicted by a simple dielectric model. The SO peak frequency decreased to $\approx 93.1\%$ of the LPP+ frequency upon oil immersion, in agreement with the dielectric model.

ACKNOWLEDGEMENTS

We acknowledge helpful discussions with Bryan T. Spann (NIST, Applied Physics Division) on the calculation of Raman cross-sections.

APPENDIX: FURTHER INFORMATION ON DATA ANALYSIS METHODS

Some of the calculations and data analysis methods used in this study are discussed in more detail here.

1. Model for curve-fitting of Raman lines

The peak frequencies, full widths at half-maximum (FWHMs), and asymmetries of the observed Raman lines, and the uncertainties of these parameters, were quantified by a nonlinear least-squares curve-fitting method. The overall model function used for curve-fitting of the Raman spectra is the sum of one or more line shape functions and a constant, linear, or quadratic polynomial background,

$$I_{meas}(\nu) = \sum_{j=1}^N \left(I_j(\nu) \right) + I_{bkg}(\nu) , \quad (A1)$$

where $I_{meas}(\nu)$ is the overall intensity as a function of Raman frequency (Stokes shift) ν , $I_j(\nu)$ is the line shape of the j th Raman line, and $I_{bkg}(\nu)$ is the polynomial background. The line shape function $I_j(\nu)$ has one of the following forms:

$$I_j(\nu) = I_{0,j} \cdot \exp \left\{ -\ln(2) \cdot \left(\frac{2(\nu - \nu_{0,j})}{w_{0,j}} \right)^2 \right\} \quad (\text{A2a})$$

(symmetric Gaussian form),

$$I_j(\nu) = I_{0,j} / \left[1 + \left(\frac{2(\nu - \nu_{0,j})}{w_{0,j}} \right)^2 \right] \quad (\text{A2b})$$

(symmetric Lorentzian form),

$$I_j(\nu) = \begin{cases} I_{0,j} / \left[1 + \left(\frac{2(\nu - \nu_{0,j})}{w_{-,j}} \right)^2 \right] & \text{for } \nu < \nu_0 \\ I_{0,j} / \left[1 + \left(\frac{2(\nu - \nu_{0,j})}{w_{+,j}} \right)^2 \right] & \text{for } \nu > \nu_0 \end{cases}, \quad (\text{A2c})$$

(simple asymmetric Lorentzian form), or

$$I_j(\nu) = I_{0,j} / \left[1 + \left(\frac{2(\nu - \nu_{0,j})}{w_{0,j}^*(\nu)} \right)^2 \right]$$

$$\text{with } w_{0,j}^*(\nu) = 0.5 \cdot [(w_{+,j}^* + w_{-,j}^*) + (w_{+,j}^* - w_{-,j}^*) \operatorname{erf}(\sqrt{\pi}(\nu - \nu_{0,j})/s_j)] \quad (\text{A2d})$$

(graded asymmetric Lorentzian form).

For the simple asymmetric Lorentzian, $(0.5 \cdot w_{+,j})$ is the upper half width at half-maximum (HWHM) (i.e., the HWHM on the high-frequency side of the peak) and $(0.5 \cdot w_{-,j})$ is the lower HWHM. The following relations then hold:

$$w_{0,j} = 0.5 \cdot (w_{+,j} + w_{-,j}) \quad (\text{A3a})$$

and

$$w_{A,j} = 0.5 \cdot (w_{+,j} - w_{-,j}), \quad (\text{A3b})$$

where $w_{0,j}$ is the FWHM and $w_{A,j}$ is the width asymmetry, defined as the difference between the upper and lower HWHM.

The graded asymmetric Lorentzian was designed to provide more accurate fits to the measured LPP+ lines than the simple asymmetric Lorentzian. In some cases, when the simple asymmetric Lorentzian is used to fit a measured LPP+ line, a significant (above the noise level) deviation between the data and fit occurs near the peak of the line. The second and higher derivatives of the simple asymmetric Lorentzian are discontinuous at the peak frequency. The tendency of the simple asymmetric Lorentzian to deviate from the measured line shape near the peak may be related to this discontinuity. In contrast, the graded asymmetric Lorentzian is infinitely differentiable at all frequencies.

For the graded asymmetric Lorentzian, the width parameter $w_{0,j}^*(\nu)$ is frequency-dependent and varies smoothly between high-frequency ($w_{+,j}^*$) and low-frequency ($w_{-,j}^*$) asymptotic values. The parameter s_j represents the width of the transition between the high-frequency and low-frequency asymptotes. The fit parameters $(0.5 \cdot w_{+,j}^*)$ and $(0.5 \cdot w_{-,j}^*)$ are not equal to the upper and lower HWHMs of the graded asymmetric Lorentzian. Instead, the upper and lower HWHMs are found by numerically solving the following equations:

$$I_j(\nu_{0,j} + 0.5 \cdot w_{+,j}) = I_j(\nu_{0,j} - 0.5 \cdot w_{-,j}) = 0.5 \cdot I_{0,j} \quad . \quad (A4)$$

Once $w_{+,j}$ and $w_{-,j}$ are determined, the FWHM and width asymmetry of the graded asymmetric Lorentzian are obtained from Eqs. (A3a) and (A3b).

The graded asymmetric Lorentzian form was used to fit the measured LPP+ lines for all samples except B738 and D270, where the simple asymmetric Lorentzian was used because the

graded form did not improve the accuracy of the fits. The measured SO lines were fitted with either the graded or simple asymmetric Lorentzian form.

2. Uncertainties of peak frequencies and other line shape parameters

As shown in Table II, several Raman spectra were measured for each growth run; the number of spectra measured for a particular growth run is denoted η . Peak frequencies and other line shape parameters were quantified by curve-fitting of the Raman spectra, as discussed above. The average value of each parameter for a given growth run was estimated by taking the average of the η curve-fitting results. Let χ_j be the value of parameter χ found by curve-fitting of the j th Raman spectrum from a given growth run, and let χ_{avg} be the average value of χ_j . In this section, a method is presented for estimating the expanded uncertainty (corresponding to a 95 % confidence interval⁴⁰) of χ_{avg} , which is denoted $U(\chi_{avg})$. The best estimate of $U(\chi_{avg})$ is assumed to be the larger of two distinct estimates obtained with different methods:

$$U(\chi_{avg}) = \max(U_{intra}(\chi_{avg}), U_{stat}(\chi_{avg})) \quad (A5)$$

where $U_{intra}(\chi_{avg})$ is called the intra-spectral uncertainty and $U_{stat}(\chi_{avg})$ is called the statistical uncertainty. These terms are defined as follows.

The uncertainty of χ_j for one Raman spectral measurement is denoted $U_{intra}(\chi_j)$. The main component of $U_{intra}(\chi_j)$, denoted the curve-fitting uncertainty $U_{cf}(\chi_j)$, depends on the deviation between the data and the fit function, which can arise from random noise or systematic error (imperfect description of the data by the fit function). The curve-fitting uncertainty $U_{cf}(\chi_j)$ was evaluated with the functions named “nlinfit” and “nlparci” in the Statistics Toolbox of the Matlab²⁶ numerical computing software. If the parameter χ represents a peak frequency

(e.g., ν_{LPP+}), then a fixed uncertainty of 0.1 cm^{-1} , which represents the error due to the drift of the Raman wavenumber calibration, is added in quadrature to $U_{cf}(\chi_j)$. The typical magnitude of the wavenumber calibration error was estimated from experiments in which the calibration procedure was repeated at regular time intervals. To first order, the calibration drift causes a constant shift of the wavenumber scale, and affects peak frequencies but not linewidths. Thus,

$$U_{intra}(\chi_j) = [U_{cf}^2(\chi_j) + \delta^2]^{1/2} \quad (\text{A6})$$

where $\delta = 0.1 \text{ cm}^{-1}$ for peak frequencies, $\delta = 0$ for other types of fit parameters. (Note that the wavenumber calibration drift term was omitted when calculating the frequency differences in the UV illumination experiment ($\Delta\nu_{LPP+}$ and $\Delta\nu_{SO}$ in Table V). The reason for this omission is that measurements of a given sample with no, low, and high UV illumination were performed a few minutes apart, which is shorter than the time scale of the wavenumber calibration drift.)

The intra-spectral estimate of the uncertainty of χ_{avg} is then calculated by averaging the squared uncertainties of the η individual measurements, $U_{intra}(\chi_j)$:

$$\begin{aligned} U_{intra}(\chi_{avg}) &= \frac{1}{\eta} \left\{ \sum_{j=1}^{\eta} U_{intra}^2(\chi_j) \right\}^{1/2} \\ &= \frac{1}{\eta} \left\{ \sum_{j=1}^{\eta} [U_{cf}^2(\chi_j) + \delta^2] \right\}^{1/2} = (\eta)^{-1/2} [U_{cf,RMS}^2 + \delta^2]^{1/2} \end{aligned} \quad (\text{A7})$$

where $U_{cf,RMS}$ is the root-mean-squared value of $U_{cf}(\chi_j)$.

The statistical uncertainty, $U_{stat}(\chi_{avg})$, is determined from the variation of χ_j within the set of η fitted values (thus, $U_{stat}(\chi_{avg})$ is undefined for $\eta = 1$). The sample standard deviation $\sigma_s(\chi)$ is calculated, then the standard error of the mean is found by multiplying by $(\eta)^{-1/2}$, then

the uncertainty corresponding to a 95 % confidence interval is found by multiplying by a “coverage factor” $T_{95}(\eta - 1)$ that is inversely related to the Student’s t distribution⁴⁰:

$$U_{stat}(\chi_{avg}) = \sigma_s(\chi) \cdot T_{95}(\eta - 1) \cdot (\eta)^{-1/2} . \quad (A8)$$

The calculated ratio of the 95 % confidence interval to the sample standard deviation, which from Eq. (A8) is $T_{95}(\eta - 1) \cdot (\eta)^{-1/2}$, decreases from 2.484 to 0.380 as η increases from 3 to 29. From Eqs. (A7) and (A8), it is seen that both $U_{intra}(\chi_{avg})$ and $U_{stat}(\chi_{avg})$ scale with η as $(\eta)^{-1/2}$. Note that $T_{95}(\eta - 1)$ is calculated with the assumption that the underlying probability distribution is Gaussian; the calculated values of $T_{95}(\eta - 1)$ and hence $U_{stat}(\chi_{avg})$ will not be correct for a non-Gaussian distribution.

Because U_{intra} is defined while U_{stat} is undefined for $\eta = 1$, it can be speculated that $U_{intra}(\chi_{avg})$ is a more accurate estimate than $U_{stat}(\chi_{avg})$ for small values of η . Thus, taking the best overall uncertainty estimate to be the maximum of $U_{intra}(\chi_{avg})$ and $U_{stat}(\chi_{avg})$ (Eq. (A5)) reduces the chances of significantly underestimating $U(\chi_{avg})$ for small η , at the expense of introducing a slight bias toward overestimation.

The two uncertainty estimates, $U_{intra}(\chi_{avg})$ and $U_{stat}(\chi_{avg})$, are expected to converge to the same value for large η (i.e., the “uncertainty of the uncertainty” decreases with increasing η) provided that two conditions are met: the underlying probability distribution is Gaussian, and the experimental conditions are the same for all measurements, i.e., there is no “inhomogeneous broadening”. Inhomogeneous broadening (i.e., some systematic variation of the experimental conditions between measurements) will cause $U_{stat}(\chi_{avg})$ to increase relative to $U_{intra}(\chi_{avg})$, because by definition $U_{intra}(\chi_{avg})$ cannot account for systematic variation between measurements. For a non-Gaussian probability distribution, the calculated coverage factor may

be either larger or smaller than the actual coverage factor. In cases where the underlying probability distribution is Gaussian, but inhomogeneous broadening occurs, the contribution to the total uncertainty $U(\chi_{avg})$ from the inhomogeneity of χ , denoted $U_{inhomog}(\chi_{avg})$, can be estimated as follows:

$$\begin{aligned} U_{inhomog}^2(\chi_{avg}) &= U^2(\chi_{avg}) - U_{intra}^2(\chi_{avg}) \\ &= \left[\max(U_{intra}(\chi_{avg}), U_{stat}(\chi_{avg})) \right]^2 - U_{intra}^2(\chi_{avg}) . \end{aligned} \quad (A9)$$

The hypothesis that $U_{intra}(\chi_{avg})$ and $U_{stat}(\chi_{avg})$ approach the same value for large η , under the conditions stated above, was confirmed with experimental results from this study. The experimental test utilized the fitted line shape parameters (peak frequency, FWHM, and width asymmetry; see Eqs. (A3a) and (A3b)) of the $A_1(TO)$, $E_1(TO)$, and E_2^{high} GaN peaks and the Si substrate peak. The line shapes of these peaks do not show any obvious sample-to-sample variation. Therefore, an uncertainty analysis of these parameters was performed with the assumption that all measurements of all samples are measurements of the same underlying parameters; 124 spectra in all were included in the analysis ($\eta = 124$). The calculated values of $U_{intra}(\chi_{avg})$ and $U_{stat}(\chi_{avg})$ were found to be in good agreement for the FWHMs of the $A_1(TO)$, $E_1(TO)$, and Si substrate peaks. More specifically, the following condition was found to hold for these parameters:

$$\left| \frac{U_{stat}(\chi_{avg}) - U_{intra}(\chi_{avg})}{0.5(U_{stat}(\chi_{avg}) + U_{intra}(\chi_{avg}))} \right| \leq \eta^{-0.5} . \quad (A10)$$

For the other parameters examined in this test, $U_{stat}(\chi_{avg})$ was found to be larger than $U_{intra}(\chi_{avg})$, as expected when significant inhomogeneous broadening occurs.

As discussed in the main text, in some cases the relevant confidence interval is not the interval that contains the mean value of χ with 95 % probability, but rather the larger interval that contains an individual measurement of χ (which can be thought of as the “next future measurement”) with 95 % probability. This larger interval, denoted $W(\chi_{avg})$, is equal to $(\eta)^{1/2} \cdot U(\chi_{avg})$. While $U(\chi_{avg})$ scales as $(\eta)^{-1/2}$, $W(\chi_{avg})$ approaches a non-zero constant value for large η .

In some experiments, such as the “scraping” experiment described in Table VI and the related discussion, the final measurement result is an average of η differences of “paired” values, $(\Delta\chi_{12})_{avg} = (\chi_1 - \chi_2)_{avg}$. The intra-spectral estimate of the uncertainty of $(\chi_1 - \chi_2)_{avg}$ is

$$U_{intra}((\chi_1 - \chi_2)_{avg}) = \frac{1}{\eta} \left\{ \sum_{j=1}^{\eta} [U_{cf}^2(\chi_{1j}) + U_{cf}^2(\chi_{2j}) + 2\delta^2] \right\}^{1/2} \quad (A11)$$

and the corresponding statistical uncertainty estimate is

$$U_{stat}((\chi_1 - \chi_2)_{avg}) = T_{95}(\eta - 1) \cdot (\eta)^{-1/2} \cdot \sigma_s(\chi_1 - \chi_2) . \quad (A12)$$

Note that the intra-spectral uncertainty is the same for the difference of averages, $(\chi_{1,avg} - \chi_{2,avg})$, as for the average of differences, $(\chi_1 - \chi_2)_{avg}$. On the other hand, if the paired values (χ_{1j}, χ_{2j}) vary in a correlated manner, then the variance of the differences $(\chi_{1j} - \chi_{2j})$ will be less than the variance of the individual values. In this case, U_{stat} will be smaller for the average of differences than for the difference of averages, i.e.,

$$U_{stat}((\chi_1 - \chi_2)_{avg}) < \left(U_{stat}^2(\chi_{1,avg}) + U_{stat}^2(\chi_{2,avg}) \right)^{1/2} . \quad (A13)$$

The uncertainties of Δv_{LPP+} shown in the rows of Table VI labeled “B738(avg)” and “B982(avg)” are examples of this case.

3. Uncertainty analysis of carrier concentration

The uncertainty of the carrier concentration N for a single Raman measurement, denoted $U(N)$, is found from Eq. (4) with use of the “chain rule” for propagation of error (for conciseness, in the following discussion ν_{LPP+} is written as ν_+):

$$U^2(N) = \left(\frac{N}{m^*}\right)^2 U^2(m^*) + \left(\frac{N}{\epsilon_\infty}\right)^2 U^2(\epsilon_\infty) \quad (\text{A14a})$$

$$+ \left(\frac{\partial N}{\partial \nu_{LO}}\right)^2 U^2(\nu_{LO}) + \left(\frac{\partial N}{\partial \nu_{TO}}\right)^2 U^2(\nu_{TO}) + \left(\frac{\partial N}{\partial \nu_+}\right)^2 U_{intra}^2(\nu_+) ,$$

where N is a function of the parameters $(m^*, \epsilon_\infty, \nu_{LO}, \nu_{TO}, \nu_+)$, the uncertainties of these parameters are denoted $U(m^*), \dots, U(\nu_+)$, and the partial derivatives in Eq. (A14a) are

$$\frac{\partial N}{\partial \nu_{LO}} = -2Km^*\epsilon_\infty \frac{\nu_{LO} \cdot \nu_+^2}{(\nu_+^2 - \nu_{TO}^2)} , \quad (\text{A14b})$$

$$\frac{\partial N}{\partial \nu_{TO}} = 2Km^*\epsilon_\infty \frac{\nu_{TO} \cdot \nu_+^2 (\nu_+^2 - \nu_{LO}^2)}{(\nu_+^2 - \nu_{TO}^2)^2} , \quad (\text{A14c})$$

and

$$\frac{\partial N}{\partial \nu_+} = 2Km^*\epsilon_\infty \frac{\nu_+ (\nu_+^4 - 2\nu_+^2 \cdot \nu_{TO}^2 + \nu_{LO}^2 \cdot \nu_{TO}^2)}{(\nu_+^2 - \nu_{TO}^2)^2} . \quad (\text{A14d})$$

Similarly, the uncertainty of the prefactor P that relates N to $(\nu_+ - \nu_{LO})$ in the linearized expression for N (Eqs. (5a) and (5b)) is

$$U^2(P) = \left(\frac{P}{m^*}\right)^2 U^2(m^*) + \left(\frac{P}{\epsilon_\infty}\right)^2 U^2(\epsilon_\infty)$$

$$+ \left(\frac{\partial P}{\partial \nu_{LO}}\right)^2 U^2(\nu_{LO}) + \left(\frac{\partial P}{\partial \nu_{TO}}\right)^2 U^2(\nu_{TO}) , \quad (\text{A15a})$$

where

$$\frac{\partial P}{\partial \nu_{LO}} = P \cdot \left[\frac{\nu_{LO}^2 - 3\nu_{TO}^2}{\nu_{LO}(\nu_{LO}^2 - \nu_{TO}^2)} \right] \quad (\text{A15b})$$

and

$$\frac{\partial P}{\partial \nu_{TO}} = P \cdot \left(\frac{2\nu_{TO}}{\nu_{LO}^2 - \nu_{TO}^2} \right) . \quad (\text{A15c})$$

To find an expression for the uncertainty of the average carrier concentration within a set of η measurements, $U(N_{avg})$ (analogous to the expression for $U(\chi_{avg})$ given by Eqs. (A5), (A7), and (A8)), first note that $N_{avg} = \frac{1}{\eta} \sum_{j=1}^{\eta} (N_j)$ is a function of the material properties parameters (m^* , ϵ_{∞} , ν_{LO} , ν_{TO}), which are the same for all measurements, and of the LPP+ frequencies $\{\nu_{+,j}\}$, which differ between measurements. In other words, the variation of N_j within the measurement set is entirely due to the variation of $\nu_{+,j}$. Three components of the uncertainty $U(N_{avg})$ can then be defined:

- (a) a “material properties” component, denoted $U_{mater}(N_{avg})$, which is derived from the uncertainties of the fixed parameters (m^* , ϵ_{∞} , ν_{LO} , ν_{TO}), and is unrelated to the variation of N_j between measurements;
- (b) an “intra-spectral” component, denoted $U_{intra}(N_{avg})$, which is derived from the “intra-spectral” uncertainties of the LPP+ frequencies ($U_{intra}(\nu_{+,j})$, see Eq. (A6));
- (c) a “statistical” component, denoted $U_{stat}(N_{avg})$, which is directly determined from the variation of N_j between measurements.

Both $U_{stat}(N_{avg})$ and $U_{intra}(N_{avg})$ are estimates of the part of $U(N_{avg})$ that arises from the uncertainties of the LPP+ frequencies; i.e. $U_{stat}(N_{avg})$ and $U_{intra}(N_{avg})$ are related to each

other in the same way as $U_{stat}(\chi_{avg})$ and $U_{intra}(\chi_{avg})$ (as defined in Eqs. (A7) and (A8)). The total uncertainty $U(N_{avg})$ is given by an expression analogous to Eq. (A5):

$$U^2(N_{avg}) = U_{mater}^2(N_{avg}) + \left[\max(U_{intra}(N_{avg}), U_{stat}(N_{avg})) \right]^2, \quad (\text{A16a})$$

where

$$U_{mater}^2(N_{avg}) = \left(\frac{N_{avg}}{m^*} \right)^2 U^2(m^*) + \left(\frac{N_{avg}}{\varepsilon_\infty} \right)^2 U^2(\varepsilon_\infty) + \frac{1}{\eta^2} \left[\left(\sum_{j=1}^{\eta} \frac{\partial N_j}{\partial v_{LO}} \right)^2 U^2(v_{LO}) + \left(\sum_{j=1}^{\eta} \frac{\partial N_j}{\partial v_{TO}} \right)^2 U^2(v_{TO}) \right], \quad (\text{A16b})$$

$$U_{intra}(N_{avg}) = \frac{1}{\eta} \left[\sum_{j=1}^{\eta} \left(\frac{\partial N_j}{\partial v_{+,j}} \right)^2 U^2(v_{+,j}) \right]^{1/2} = (\eta)^{-1/2} \left[\left(\frac{\partial N_j}{\partial v_{+,j}} \right) U(v_{+,j}) \right]_{rms}, \quad (\text{A16c})$$

and $U_{stat}(N_{avg})$ is defined by the analogous equation to Eq. (A8). The dominant terms of $U_{mater}(N_{avg})$ arise from the uncertainties of m^* and ε_∞ (the material properties parameters contained in the prefactor \mathbf{K} defined in Eq. (3)). Thus, the following expression is a good approximation to $U_{mater}(N_{avg})$:

$$U_{mater}(N_{avg}) \approx \left[\left(\frac{U(m^*)}{m^*} \right)^2 + \left(\frac{U(\varepsilon_\infty)}{\varepsilon_\infty} \right)^2 \right]^{1/2} \cdot N_{avg} = 0.0535 \cdot N_{avg} \quad (\text{A16d})$$

According to the above definitions, $U_{intra}(N_{avg})$ and $U_{stat}(N_{avg})$ scale with the number of measurements as $(\eta)^{-1/2}$. On the other hand, provided that the approximation of Eq. (A16d) is accurate, $U_{mater}(N_{avg})$ is independent of η and is directly proportional to N_{avg} . Thus, $U_{mater}(N_{avg})$ will be the dominant component of $U(N_{avg})$, and the approximation $U(N_{avg})/N_{avg} \gtrsim 0.0535$ will hold, for a sufficiently large number of measurements or for sufficiently high carrier concentration. From Table II, $U(N_{avg})/N_{avg} = 0.057$ for the sample

with the highest carrier approximation, sample D270; this result confirms that $U_{mater}(N_{avg})$ is the dominant uncertainty component for D270.

$U(N_{avg})$ can also be expressed as the quadrature sum of three components:

$$U^2(N_{avg}) = U_{mater}^2(N_{avg}) + U_{intra}^2(N_{avg}) + U_{inhomog}^2(N_{avg}) , \quad (A17a)$$

where (analogous to Eq. (A9)) the component due to the inhomogeneity of N is

$$U_{inhomog}^2(N_{avg}) = \left[\max(U_{intra}(N_{avg}), U_{stat}(N_{avg})) \right]^2 - U_{intra}^2(N_{avg}) . \quad (A17b)$$

As discussed in the main text, in some cases the relevant measure of the uncertainty of N is not the uncertainty corresponding to the interval than contains the true mean value of N (denoted N_{mean} , where $N_{mean} \rightarrow N_{avg}$ as $\eta \rightarrow \infty$) with 95 % probability, but rather the uncertainty corresponding to the larger interval that contains an individual measurement of N (which can be thought of as the “next future measurement”) with 95 % probability. The latter uncertainty, denoted $W(N_{avg})$, is found by multiplying the uncertainty components that are correlated with the variation of N between measurements by the factor $(\eta)^{1/2}$:

$$\begin{aligned} W^2(N_{avg}) &= U_{mater}^2(N_{avg}) + \eta \cdot \left[\max(U_{intra}(N_{avg}), U_{stat}(N_{avg})) \right]^2 \\ &= U_{mater}^2(N_{avg}) + \eta \cdot U_{intra}^2(N_{avg}) + \eta \cdot U_{inhomog}^2(N_{avg}) \\ &= U_{mater}^2(N_{avg}) + W_{intra}^2(N_{avg}) + W_{inhomog}^2(N_{avg}) . \end{aligned} \quad (A18)$$

Each of the components of $W(N_{avg})$ approaches a fixed non-zero value as $\eta \rightarrow \infty$.

$U_{mater}(N_{avg})$ is the dominant component of $W(N_{avg})$, and (see Eq. (A16d)) the approximation $W(N_{avg})/N_{avg} \gtrsim 0.0535$ will be accurate, for sufficiently high carrier concentration.

An expression for the uncertainty of the difference between two carrier concentration measurements, $\Delta N_{12} \equiv N_1 - N_2$, is needed for uncertainty analysis of some of the experimental results. The expression for $U(\Delta N_{12})$ is similar to the expression for $U(N)$ (Eq. (A14)):

$$U^2(\Delta N_{12}) = \left(\frac{\Delta N_{12}}{m^*}\right)^2 U^2(m^*) + \left(\frac{\Delta N_{12}}{\varepsilon_\infty}\right)^2 U^2(\varepsilon_\infty) + \left(\frac{\partial(N_1-N_2)}{\partial v_{LO}}\right)^2 U^2(v_{LO}) \quad (\text{A19})$$

$$+ \left(\frac{\partial(N_1-N_2)}{\partial v_{TO}}\right)^2 U^2(v_{TO}) + \left(\frac{\partial N_1}{\partial v_{1+}}\right)^2 U^2(v_{1+}) + \left(\frac{\partial N_2}{\partial v_{2+}}\right)^2 U^2(v_{2+}) .$$

Finally, an expression for the uncertainty of the average of η differences of carrier concentrations, $U^2(\Delta N_{12,avg})$, is useful in some cases, such as the calculation of the uncertainties of ΔN shown in the rows of Table VI labeled “B738(avg)” and “B982(avg)”:

$$U^2(\Delta N_{12,avg}) = U_{mater}^2(\Delta N_{12,avg}) + \left[\max \left(U_{intra}(\Delta N_{12,avg}), U_{stat}(\Delta N_{12,avg}) \right) \right]^2 , \quad (\text{A20a})$$

where

$$U_{mater}^2(\Delta N_{12,avg}) = \left(\frac{\Delta N_{12,avg}}{m^*}\right)^2 U^2(m^*) + \left(\frac{\Delta N_{12,avg}}{\varepsilon_\infty}\right)^2 U^2(\varepsilon_\infty)$$

$$+ \frac{1}{\eta^2} \left[\left(\sum_{j=1}^{\eta} \left(\frac{\partial N_{1,j}}{\partial v_{LO}} - \frac{\partial N_{2,j}}{\partial v_{LO}} \right) \right)^2 U^2(v_{LO}) + \left(\sum_{j=1}^{\eta} \left(\frac{\partial N_{1,j}}{\partial v_{TO}} - \frac{\partial N_{2,j}}{\partial v_{TO}} \right) \right)^2 U^2(v_{TO}) \right] , \quad (\text{A20b})$$

$$U_{intra}^2(\Delta N_{12,avg}) = \frac{1}{\eta^2} \sum_{j=1}^{\eta} \left(\left(\frac{\partial N_{1,j}}{\partial v_{1+,j}} \right)^2 U^2(v_{1+,j}) + \left(\frac{\partial N_{2,j}}{\partial v_{2+,j}} \right)^2 U^2(v_{2+,j}) \right) , \quad (\text{A20c})$$

and $U_{stat}(\Delta N_{12,avg})$ is given by an equation analogous to Eq. (A8).

4. High-frequency dielectric constant ϵ_∞

In Sanford(2003), Ref. 20, the dispersion of n_o was measured by two methods: a prism-coupled waveguide mode (PCWM) method at discrete wavelengths of 442 nm to 1064 nm, and a spectroscopic transmittance and reflectance (STR) method within a continuous wavelength range of 370 nm to 2500 nm. The correlated PCWM and STR results were fitted by a two-term Sellmeier equation:

$$\epsilon_\perp(\lambda) = n_o^2(\lambda) = 1 + \frac{A_1}{1-(B_1/\lambda)^2} + \frac{A_2}{1-(B_2/\lambda)^2} \quad (\text{A21})$$

with parameters $A_1=0.083$, $A_2=4.085$, $B_1=354.8$ nm, and $B_2=180.3$ nm. In Eq. (A21), $\epsilon_\perp(\lambda)$ is the dielectric function for electric field perpendicular to the c -axis (corresponding to the ordinary refractive index). The fitted values at the extremes of the PCWM wavelength range are $\epsilon_\perp(442 \text{ nm}) = 6.134$, $\epsilon_\perp(1064 \text{ nm}) = 5.299$; the fitted values at the extremes of the STR range are $\epsilon_\perp(370 \text{ nm}) = 7.388$, $\epsilon_\perp(2500 \text{ nm}) = 5.191$; and the extrapolated long-wavelength limit of $\epsilon_\perp(\lambda)$ is $\epsilon_{\perp,\infty} = 5.168$.

Also in Sanford(2003), the dispersion of n_e was measured by the prism-coupled waveguide mode (PCWM) method at discrete wavelengths of 442 nm to 1064 nm and fitted by a one-term Sellmeier equation:

$$\epsilon_\parallel(\lambda) = n_e^2(\lambda) = 1 + \frac{A_e}{1-(B_e/\lambda)^2} \quad (\text{A22})$$

with $A_e=4.321$ and $B_e=189.2$ nm. In Eq. (A22), $\epsilon_\parallel(\lambda)$ is the dielectric function for electric field parallel to the c -axis (corresponding to the extraordinary refractive index). The fitted values at the extremes of the PCWM range are $\epsilon_\parallel(442 \text{ nm}) = 6.290$ and $\epsilon_\parallel(1064 \text{ nm}) = 5.462$; the extrapolated long-wavelength limit is $\epsilon_{\parallel,\infty} = 5.321$. The estimated uncertainty of each fitted value of ϵ_\perp or ϵ_\parallel is 0.025. Note that in all cases, the extrapolated long-wavelength limit of the

dielectric function lies outside the measurement range by only a small amount, compared to the span of the measurement range. For example, $\epsilon_{\parallel}(1064 \text{ nm}) - \epsilon_{\parallel,\infty} = 0.141$; this difference is only 16 % of the span of the PCWM measurements, which is $\epsilon_{\parallel}(442 \text{ nm}) - \epsilon_{\parallel}(1064 \text{ nm}) = 0.828$.)

In Pezzagna(2008), Ref. 21, the dispersions of n_o and n_e were measured by the PCWM method at discrete wavelengths of 458 nm to 1550 nm, and the results were fit by a two-term Sellmeier equation, Eq. (A21), with parameters $A_1=0.213$, $A_2=3.988$, $B_1=350 \text{ nm}$, and $B_2=153 \text{ nm}$ for n_o , and $A_1=0.118$, $A_2=4.201$, $B_1=350 \text{ nm}$, and $B_2=176.5 \text{ nm}$ for n_e . The fitted values of ϵ_{\perp} at the extremes of the wavelength range are $\epsilon_{\perp}(458 \text{ nm}) = 6.001$, $\epsilon_{\perp}(1550 \text{ nm}) = 5.252$; the extrapolated long-wavelength limit is $\epsilon_{\perp,\infty} = 5.201$. The fitted values of ϵ_{\parallel} at the extremes of the wavelength range are $\epsilon_{\parallel}(458 \text{ nm}) = 6.217$, $\epsilon_{\parallel}(1550 \text{ nm}) = 5.381$; the extrapolated long-wavelength limit is $\epsilon_{\parallel,\infty} = 5.319$.

The polarization of the scattered light was effectively randomized in the Raman measurements of NW ensembles (as discussed further below). When the difference between $\epsilon_{\parallel,\infty}$ and $\epsilon_{\perp,\infty}$ is small, as in this case, the effective value of the dielectric constant for randomized polarization can be approximated as $\epsilon_{random,\infty} = \frac{1}{3}\epsilon_{\parallel,\infty} + \frac{2}{3}\epsilon_{\perp,\infty}$. The (1/3, 2/3) weighting arises because the dielectric constant is $\epsilon_{\parallel,\infty}$ for polarization parallel to the c -axis, while the dielectric constant is $\epsilon_{\perp,\infty}$ for polarization in the plane perpendicular to the c -axis, which contains two orthogonal axes. An overall average value $\epsilon_{avg,\infty}$ was then calculated as the equal-weighted average of the values of $\epsilon_{random,\infty}$ from Sanford(2003) and Pezzagna(2008):

$$\epsilon_{avg,\infty} = \frac{1}{2} \left[\frac{1}{3}\epsilon_{\parallel,\infty}(S) + \frac{2}{3}\epsilon_{\perp,\infty}(S) \right] + \frac{1}{2} \left[\frac{1}{3}\epsilon_{\parallel,\infty}(P) + \frac{2}{3}\epsilon_{\perp,\infty}(P) \right] = 5.23 \quad , \quad (\text{A23})$$

where the labels S and P denote the results of Sanford(2003) and Pezzagna(2008), respectively. The uncertainty of $\epsilon_{avg,\infty}$ is assumed to be 0.1, which takes into account the variation between the results of the two studies, and uncertainties associated with the long-wavelength extrapolation and data averaging procedures.

5. Scattering geometry effects on Raman spectra: quasi-LO and quasi-TO phonon modes

The presence or absence of specific peaks in Raman spectroscopy measurements of wurtzite-structure GaN is governed by selection rules related to the scattering geometry, i.e., the propagation and polarization directions of the incident and scattered light. The selection rules are simplest when each propagation or polarization direction is parallel or anti-parallel to x , y , or z (\bar{x} denotes the direction anti-parallel to x), such that z is the crystal c -axis, and x and y are any two orthogonal directions in the c -plane. (Note that, because of the lack of inversion symmetry of the wurtzite crystal structure, the $[0001]$ or Ga-polarity direction is not equivalent to the $[000\bar{1}]$ or N-polarity direction. However, Raman measurements are insensitive to polarity. Thus, z can denote either the $[0001]$ or the $[000\bar{1}]$ direction.) The scattering geometry, i.e., the set of propagation and polarization directions, is commonly expressed in the notation $r_1(r_2r_3)r_4$, where r_1 is the incident propagation direction, r_2 is the incident polarization direction, r_3 is the scattered polarization direction, and r_4 is the scattered propagation direction. For example, $z(yy)\bar{z}$ denotes backscatter with propagation along the c -axis, and incident and scattered polarization parallel to each other in the c -plane. The selection rules for the first-order Raman modes of GaN are listed in Table 2 of Ref. 41.

In this study, the incident and scattered propagation directions were 65° from the surface normal, and hence $\approx 65^\circ$ from the c -axes of most NWs, because the growth direction¹ is along

the c -axis, and also the growth direction of most NWs is close to the surface normal (see Fig. 1). The accessible polarization geometries are labeled (p, p) , (s, s) , (p, s) , and (s, p) , where the first label gives the incident polarization, the second label gives the scattered-light polarization, p denotes polarization in the plane of incidence, and s denotes polarization perpendicular to the plane of incidence (and thus parallel to the sample surface). Because of the oblique incidence, these geometries do not match any of the simple experiment geometries listed in Ref. 41, but can be described as combinations of simple geometries. For example, the (s, s) configuration can be described in the standard notation as $-(yy) -$, or, equivalently, as some combination of the $x(yy)\bar{x}$, $z(yy)\bar{z}$, and $x(yy)z$ geometries. For this combination, the $A_1(TO)$, $A_1(LO)$, and E_2 modes are allowed, while the $E_1(TO)$ and $E_1(LO)$ modes are forbidden.

Raman spectra of sample D299 obtained with the (p, p) , (s, s) , (p, s) , and (s, p) polarization geometries are plotted in Fig. 10. All the first-order GaN Raman peaks are observed for all geometries, and the relative peak intensities (i.e., the intensity ratios of the peaks other than E_2^{high} to the E_2^{high} peak, which is the most intense) show little or no variation with polarization geometry. Similar results were obtained for the other samples. Thus, the Raman results for our samples are not described by the selection rules given in Ref. 41, even though the NWs are highly oriented. The absence of observable polarization dependence is ascribed to a diffusive type of elastic light scattering within the NW ensembles, which leads to essentially complete randomization of the optical polarization and propagation directions for both the incident and Raman-shifted wavelengths. The diffusive elastic scattering occurs because adjacent NWs in the ensembles are separated by air gaps, as seen in the plan-view micrographs of Fig. 1, and the refractive index difference between the NWs ($n \approx 2.4$) and air ($n = 1$) is large.

In contrast to the absence of polarization dependence for the NW samples, Raman measurements in our spectrometer of *c*-axis oriented GaN films with (approximately) optically flat surfaces showed a strong polarization dependence, consistent with the selection rules described above. The latter result supports the hypothesis that diffusive light scattering plays a critical role in randomizing the polarization during Raman measurements of the NW ensembles, because this type of scattering does not occur in continuous films with optically flat surfaces.

As illustrated in Figs. 2(b) and 3, a single LO phonon or LPP+ peak was observed in all the samples in this study, from undoped (C024) to most heavily doped (D270); the $A_1(LO)$ and $E_1(LO)$ phonon peaks, which have been reported^{22,27,28} in Raman studies of single-crystal wurtzite-structure GaN, were not resolved. The observation of a single LO phonon peak in undoped NW material (such as C024), with intermediate frequency between the $A_1(LO)$ and $E_1(LO)$ peaks, is attributed to randomization of the optical polarization and propagation directions, and hence also the phonon propagation direction, by the diffusive light scattering mechanism discussed above. According to previous modeling⁴² and experimental^{43,44,45} studies, “mixed” LO phonon modes with frequencies between $\nu_{A_1(LO)}$ and $\nu_{E_1(LO)}$, as well as “mixed” TO phonon modes with frequencies between $\nu_{A_1(TO)}$ and $\nu_{E_1(TO)}$, occur for phonon propagation directions between parallel and perpendicular to the *c*-axis. These mixed modes are called quasi-LO or quasi-TO modes in the literature; we will use these terms from hereon. The occurrence of quasi-LO modes in the Raman spectra of GaN NW ensembles was previously hypothesized in Ref. 6 (Fig. 5 and related discussion).

The frequencies of the quasi-LO phonon modes, as well as the “endpoint” $A_1(LO)$ and $E_1(LO)$ modes, are expressed as

$$\left(\nu_{quasi-LO}(\theta)\right)^2 = \left(\nu_{A_1(LO)}\right)^2 \cos^2(\theta) + \left(\nu_{E_1(LO)}\right)^2 \sin^2(\theta) , \quad (A24)$$

where θ is the angle between the phonon propagation direction and the c -axis, $\theta = 0$ corresponds to the $A_1(LO)$ endpoint, and $\theta = 90^\circ$ corresponds to the $E_1(LO)$ endpoint. The frequencies of the quasi-TO modes are given by the analogous expression. The weighted-average LO or TO phonon frequency for a random mixture of propagation directions, $\nu_{quasi,avg}$, is then given by the integral expression

$$\nu_{quasi,avg} = \int_0^\pi d\theta \left(\frac{\sin(\theta)}{2} \right) \left\{ (\nu_{A_1})^2 \cos^2(\theta) + (\nu_{E_1})^2 \sin^2(\theta) \right\}^{1/2} \quad (A25)$$

where the weighting factor $\left(\frac{\sin(\theta)}{2} \right)$ accounts for the fact that a greater range of propagation directions is available perpendicular to the c -axis ($\theta = 90^\circ$) than parallel or anti-parallel to the c -axis ($\theta = 0^\circ$ or $\theta = 180^\circ$).

The integral expression can be simplified by defining $u = \cos(\theta)$, $\nu_0 = \frac{1}{3}\nu_{A_1} + \frac{2}{3}\nu_{E_1}$, and $x = (\nu_{E_1} - \nu_{A_1})/(\nu_{A_1} + 2\nu_{E_1})$, and noting that the integrand is an even function of u :

$$\nu_{quasi,avg} = \nu_0 \int_0^1 du \{ (1 - 2x)^2 u^2 + (1 + x)^2 (1 - u^2) \}^{1/2} \quad (A26)$$

This integral has a closed-form solution. However, a simple and accurate approximate solution is found by noting that $x \ll 1$ (more specifically, $x = 0.0032$ for the quasi-LO modes, $x = 0.0163$ for the quasi-TO modes), and expanding the integrand as a Taylor series in x :

$$\nu_{quasi,avg} \approx \nu_0 \int_0^1 du \left\{ 1 + (1 - 3u^2)x + \frac{9}{2}(u^2 - u^4)x^2 \right\} = \nu_0 \left(1 + \frac{3}{5}x^2 \right) \quad (A27)$$

References

-
- ¹ K.A. Bertness, N.A. Sanford, and A.V. Davydov, “GaN Nanowires Grown by Molecular Beam Epitaxy”, *IEEE J Sel Top Quantum Electron* **17**, 847 (2011)
- ² S. Arafin, “Review of recent progress of III-nitride nanowire lasers”, *J Nanophotonics* **7**, 074599 (2013)
- ³ G. Irmer, V.V. Toporov, B.H. Bairamov, and J. Monecke, “Determination of the charge carrier concentration and mobility in n-GaP by Raman spectroscopy”, *Phys Stat Sol B* **119**, 595 (1983)
- ⁴ K. Jeganathan, R.K. Debnath, R. Meijers, T. Stoica, R. Calarco, D. Grützmacher, and H. Lüth, “Raman scattering of phonon-plasmon coupled modes in self-assembled GaN nanowires”, *J Appl Phys* **150**, 123707 (2009)
- ⁵ D. Wang, C.-C. Tin, J.R. Williams, M. Park, Y.S. Park, C.M. Park, T.W. Kang, and W.-C. Yang, “Raman characterization of electronic properties of self-assembled GaN nanorods grown by plasma-assisted molecular-beam epitaxy”, *Appl Phys Lett* **87**, 242105 (2005)
- ⁶ T. Stoica and R. Calarco, “Doping of III-Nitride Nanowires Grown by Molecular Beam Epitaxy”, *IEEE J Sel Top Quantum Electron* **17**, 859 (2011)
- ⁷ T. Kozawa, T. Kachi, H. Kano, Y. Taga, M. Hashimoto, N. Koide, and K. Manabe, “Raman scattering from LO phonon-plasmon coupled modes in gallium nitride”, *J Appl Phys* **75**, 1098 (1994)
- ⁸ R. Katayama, Y. Kuge, K. Onabe, T. Matsushita, and T. Kondo, “Complementary analyses on the local polarity in lateral polarity-inverted GaN heterostructure on sapphire (0001) substrate”, *Appl Phys Lett* **89**, 231910 (2006)
- ⁹ C. Wetzel, W. Walukiewicz, E.E. Haller, J. Ager III, I. Grzegory, S. Porowski, and T. Suski, “Carrier localization of as-grown n-type gallium nitride under large hydrostatic pressure”, *Phys Rev B* **53**, 1322 (1996)
- ¹⁰ M. Yoon, I.-W. Park, H. Choi, S.S. Park, and E.K. Koh, “Free Carrier Concentration Gradient along the c-Axis of a Freestanding Si-doped GaN Single Crystal”, *Jpn J Appl Phys* **44**, 828 (2005)
- ¹¹ R. Cuscó, N. Domènech-Amador, L. Artús, T. Gotschke, K. Jeganathan, T. Stoica, and R. Calarco, “Probing the electron density in undoped, Si-doped, and Mg-doped InN nanowires by means of Raman scattering”, *Appl Phys Lett* **97**, 221906 (2010)
- ¹² P. Parkinson, C. Dodson, H. J. Joyce, K.A. Bertness, N.A. Sanford, L.M. Herz, and M.B. Johnston, “Noncontact Measurement of Charge Carrier Lifetime and Mobility in GaN Nanowires”, *NanoLett* **12**, 4600 (2012)

-
- ¹³ J.L. Bolland, S. Conesa-Boj, P. Parkinson, G. Tütüncüoglu, F. Matteini, D. Rüffer, A. Casadei, F. Amaduzzi, F. Jabeen, C.L. Davies, H.J. Joyce, L.M. Herz, A. Fontcuberta-i-Morrall, and M.B. Johnston, “Modulation Doping of GaAs/AlGaAs Core–Shell Nanowires With Effective Defect Passivation and High Electron Mobility”, *NanoLett* **15**, 1336 (2015)
- ¹⁴ B. Ketterer, E. Uccelli, and A. Fontcuberta-i-Morrall, “Mobility and carrier density in p-type GaAs nanowires measured by transmission Raman spectroscopy”, *Nanoscale* **4**, 1789 (2012)
- ¹⁵ F. Wang, Q. Gao, K. Peng, Zhe Li, Ziyuan Li, Y. Guo, L. Fu, L.M. Smith, H.H. Tan, and C. Jagadish, “Spatially Resolved Doping Concentration and Nonradiative Lifetime Profiles in Single Si-Doped InP Nanowires Using Photoluminescence Mapping”, *NanoLett* **15**, 3017 (2015)
- ¹⁶ V. Laneuville, F. Demangeot, R.P´echou, P. Salles, A. Ponchet, K. March, L.F. Zagonel, and R. Songmuang, “Double strain state in a single GaN/AlN nanowire: Probing the core-shell effect by ultraviolet resonant Raman scattering”, *Phys Rev B* **83**, 115417 (2011)
- ¹⁷ P.J. Pauzauskie, D. Talaga, Kwanyong Seo, Peidong Yang, and F. Francois Lagugne´-Labarthe, “Polarized Raman Confocal Microscopy of Single Gallium Nitride Nanowires”, *J Am Chem Soc* **127**, 17146 (2010)
- ¹⁸ N.A. Sanford, L.H. Robins, P.T. Blanchard K. Soria, B. Klein, B.S. Eller, K.A. Bertness, J.B. Schlager, and A.W. Sanders, “Studies of photoconductivity and field effect transistor behavior in examining drift mobility, surface depletion, and transient effects in Si-doped GaN nanowires in vacuum and air”, *J Appl Phys* **113**, 174306 (2013)
- ¹⁹ I. Vurgaftman and J.R. Meyer, “Band parameters for nitrogen-containing semiconductors”, *J Appl Phys* **94**, 3675 (2003)
- ²⁰ N.A. Sanford, L.H. Robins, A.V. Davydov, A. Shapiro, D.V. Tsvetkov A.V. Dmitriev, S. Keller, U.K. Mishra, and S.P. DenBaars, “Refractive index study of Al_xGa_{1-x}N films grown on sapphire substrates”, *J Appl Phys* **94**, 2980 (2003)
- ²¹ S. Pezzagna, J. Brault, M. Leroux, J. Massies, and M. de Micheli, “Refractive indices and elasto-optic coefficients of GaN studied by optical waveguiding”, *J Appl Phys* **103**, 123112 (2008)
- ²² V.Yu. Davydov, Yu.E. Kitaev, I.N. Goncharuk, A.N. Smirnov, J. Graul, O. Semchinova, D. Uffmann, M B. Smirnov, A.P. Mirgorodsky, and R.A. Evarestov, “Phonon dispersion and Raman scattering in hexagonal GaN and AlN”, *Phys Rev B* **58**, 12899 (1998)
- ²³ K.A. Bertness, A. Roshko, L.M. Mansfield, T.E. Harvey, and N.A. Sanford “Mechanism for spontaneous growth of GaN nanowires with molecular beam epitaxy”, *J Cryst Growth* **310**, 3154 (2008)

-
- ²⁴ C.T. Foxon, I. Harrison, S.V. Novikov, A.J. Winsor, R.P. Campion, and T. Li, "The growth and properties of GaN:As layers prepared by plasma-assisted molecular beam epitaxy", *J. Phys.: Condens. Matter* **14**, 3383 (2002)
- ²⁵ K.A. Bertness, M.D. Brubaker, T.E. Harvey, S.M. Duff, A.W. Sanders, and N.A. Sanford, "In situ temperature measurements for selective epitaxy of GaN nanowires," *Phys Stat Solidi C* **11**, 590 (2014)
- ²⁶ Commercial equipment, instruments, or materials are identified only in order to adequately specify certain procedures. In no case does such identification imply recommendation or endorsement by the National Institute of Standards and Technology, nor does it imply that the products identified are necessarily the best available for the purpose.
- ²⁷ T. Azuhata, T. Sota, K. Suzuki, and S. Nakamura, "Polarized Raman spectra in GaN", *J Phys: Condens Matter* **7**, L129 (1995)
- ²⁸ H. Siegle, G. Kaczmarczyk, L. Filippidis, A.P. Litvinchuk, A. Hoffmann, and C. Thomsen, "Zone-boundary phonons in hexagonal and cubic GaN", *Phys Rev B* **55**, 7000 (1997)
- ²⁹ L.H. Dubois and G.P. Schwartz, "Surface optical phonons and hydrogen chemisorption on polar and nonpolar faces of GaAs, GaP, and InP", *Phys Rev B* **26**, 794 (1982)
- ³⁰ H.C. Guo, X.H. Zhang, W. Liu, A.M. Yong, and S.H. Tang, "Terahertz carrier dynamics and dielectric properties of GaN epilayers with different carrier concentrations", *J Appl Phys* **106**, 063104 ((2009)
- ³¹ L.M. Mansfield, K.A. Bertness, P.T. Blanchard, T.E. Harvey, A.W. Sanders, and N.A. Sanford, "GaN Nanowire Carrier Concentration Calculated from Light and Dark Resistance Measurements", *J Electron Mater* **38**, 495 (2009)
- ³² P.T. Blanchard, K.A. Bertness, T.E. Harvey, L.M. Mansfield, A.W. Sanders, and N.A. Sanford, "MESFETs made from individual GaN nanowires," *IEEE Trans. Nanotechnol* **7**, 760 (2008)
- ³³ A. Henning, B. Klein, K.A. Bertness, P.T. Blanchard, N.A. Sanford, and Y. Rosenwaks, "Measurement of the electrostatic edge effect in wurtzite GaN nanowires", *Appl Phys Lett* **105**, 213107 (2014)
- ³⁴ M.H. Grimsditch, D. Olego, and M. Cardona, "Absolute cross-section of first-order Raman scattering in GaAs", *Phys Rev B* **20**, 1758 (1979)
- ³⁵ I. Loa, S. Gronemeyer, C. Thomsen, O. Ambacher, D. Schikora, and D.J. As, "Comparative Determination of Absolute Raman Scattering Efficiencies and Application to GaN", *J Raman Spectrosc* **29**, 291 (1998)

-
- ³⁶ J. Wang, F. Demangeot, R. Péchou, C. Bayon, A. Mlayah, and B. Daudin, “Size and shape effects in the Raman scattering by single GaN nanowires”, *J Appl Phys* **114**, 223506 (2013)
- ³⁷ N.A. Sanford, P.T. Blanchard, K.A. Bertness, L. Mansfield, J.B. Schlager, A.W. Sanders, A. Roshko, B.B. Burton, and S.M. George, “Steady-state and transient photoconductivity in c-axis GaN nanowires grown by nitrogen-plasma-assisted molecular beam epitaxy”, *J Appl Phys* **107**, 034318 (2010)
- ³⁸ J.B. Schlager, N.A. Sanford, K.A. Bertness, J.M. Barker, A. Roshko, and P.T. Blanchard, “Polarization-resolved photoluminescence study of individual GaN nanowires grown by catalyst-free molecular beam epitaxy”, *Appl Phys Lett* **88**, 213106 (2006)
- ³⁹ J.M. Pitarke, V.M. Silkin, E.V. Chulkov, and P.M. Echenique, “Theory of surface plasmons and surface-plasmon polaritons”, *Rep Prog Phys* **70**, 1 (2007)
- ⁴⁰ D.C. Montgomery and G.C. Runger, “Applied Statistics and Probability for Engineers”, John Wiley & Sons, 1999; see in particular the following sections: 7-7 “Introduction on Confidence Intervals”, 8-3 “Inference on the Mean of a Population, Variance Unknown”, Appendix A Table IV, “Percentage Points of the t-Distribution”, Appendix B-IV, “Development of the t- and F-distributions”
- ⁴¹ H. Harima, “Properties of GaN and related compounds studied by means of Raman scattering”, *J Phys: Condens Matter* **14**, R967 (2002)
- ⁴² C.A. Arguello, D.L. Rousseau, and S.P.S. Porto, “First-order Raman effect in wurtzite-type crystals”, *Phys Rev* **181**, 1351 (1969)
- ⁴³ L. Filippidis, H. Siegle, A. Hoffmann, C. Thomsen, K. Karch, and F. Bechstedt, “Raman frequencies and angular dispersion of polar modes in aluminum nitride and gallium nitride”, *Phys Stat Sol B* **198**, 621 (1996)
- ⁴⁴ L. Bergman, M. Dutta, C. Balkas, R.F. Davis, J.A. Christman, D. Alexson, and R.J. Nemanich, “Raman analysis of the E1 and A1 quasi-longitudinal optical and quasi-transverse optical modes in wurtzite AlN”, *J Appl Phys* **85**, 3535 (1999)
- ⁴⁵ T. Azuhata, M. Ono, K. Torii, T. Sota, S.F. Chichibu, and S. Nakamura, “Forward Raman scattering by quasilongitudinal optical phonons in GaN”, *J Appl Phys* **88**, 5202 (2000)

TABLE I. Growth parameters for samples used in this study. The Ga and N fluxes are represented with the equivalent Ga-limited (N-limited) growth rate (GR) for planar growth conditions. RF is the radio-frequency power of the N₂ plasma source. See text for details of flux estimates and nucleation conditions. The seven samples from the BC growth system (C024 to C236) are listed first, followed by the five samples from the D growth system (D299 to D270). Note that C239, C144, and C236 were grown with a different Si cell and source charge than the other, earlier BC runs.

Growth run	Growth Temp. (°C)	Si Temp. (°C)	Ga GR (nm/h)	N ₂ GR (nm/h)	N ₂ flow (sccm)	RF (W)
C024	820	—	170	< 170	3	350
B738	800	—	65	> 65	3	450
C023	820	1150	170	<170	3	350
B982	805	1150	170	< 170	3	350
C239	832	1125	65	> 65	3	350
C144	818	1125	170	< 170	3	350
C236	829	1125	65	> 65	3	350
D299	800	1125	95	540	1.5	300
D260	811	1150	120	290	0.8	300
D262	807	1165	110	290	0.8	300
D273	811	1175	110	290	0.8	300
D270	805	1175	105	290	0.8	300

TABLE II. Average values of LPP+ peak frequency ($\nu_{LPP+,avg}$) and carrier concentration (N_{avg}), and number of averaged measurements (η), for each sample. The expanded uncertainties (corresponding to 95 % confidence intervals) are shown in parentheses after the parameter values. It is assumed that $N=0$ for the undoped sample C024. The column showing Si cell temperature is repeated from Table I.

Growth run	Si Temp. (°C)	$\nu_{LPP+,avg}$ (cm ⁻¹)	N_{avg} (10 ¹⁶ cm ⁻³)	η
C024	—	739.10 (0.02)	0.00 (0.11)	29
B738	—	740.47 (0.30)	5.28 (1.19)	4
C023	1150	741.15 (0.13)	7.86 (0.67)	6
B982	1150	741.93 (0.17)	10.8 (0.9)	6
C239	1125	743.90 (0.37)	18.3 (1.7)	3
C144	1125	744.58 (0.16)	20.8 (1.3)	27
C236	1125	745.92 (0.36)	25.9 (1.9)	4
D299	1125	739.65 (0.05)	2.13 (0.24)	10
D260	1150	741.35 (0.04)	8.65 (0.50)	10
D262	1165	744.27 (0.28)	19.7 (1.5)	10
D273	1175	747.98 (0.47)	33.5 (2.5)	10
D270	1175	755.73 (0.34)	61.6 (3.5)	10

TABLE III. Estimates of uncertainty of the carrier concentration for single NWs taken from sample locations near the Raman measurement locations. The overall uncertainty $W(N_{avg})$ for each sample is shown in column 2, and three components of $W(N_{avg})$ are shown in columns 3 to 5 (where $W(N_{avg})$ is equal to the quadrature sum of the three components). The first component, U_{mater} , is attributed to the uncertainties of the materials properties parameters (m^* , ϵ_∞ , ν_{LO} , ν_{TO}). The second component, W_{intra} , is attributed to “instrumental” contributions to the uncertainty of ν_{LPP+} (such as noise in the Raman measurements or wavenumber calibration drift). The third component, $W_{inhomog}$, is ascribed to the inhomogeneity of N or other material properties that determine ν_{LPP+} .

Growth run	$W(N_{avg})$ (10^{16} cm^{-3})	U_{mater}	W_{intra}	$W_{inhomog}$
C024	0.46	0.08	0.45	0
B738	2.3	0.29	0.60	2.2
C023	1.3	0.43	0.40	1.2
B982	1.6	0.59	0.42	1.5
C239	2.6	0.98	0.73	2.3
C144	3.3	1.1	0.50	3.0
C236	3.0	1.4	2.7	0
D299	0.63	0.14	0.42	0.44
D260	0.71	0.47	0.54	0
D262	3.5	1.1	0.62	3.3
D273	5.8	1.8	2.2	5.1
D270	5.0	3.3	2.0	3.2

TABLE IV. Measured values and uncertainties (shown in parentheses after the parameter values) of selected Raman line shape parameters for samples used in this study. These results were obtained by curve-fitting of the Raman spectra, following by taking the average of several measurements for each sample. The parameters listed in columns 2 to 5 are, respectively, the FWHM of the LPP+ line ($w_{0,LPP+}$), the width asymmetry of the LPP+ line ($w_{A,LPP+}$) (as defined in the Appendix part 1), the peak frequency of the SO line (ν_{SO}), and the peak frequency of a line ascribed to a local vibrational mode (ν_{LVM}).

Growth run	$w_{0,LPP+}$ (cm^{-1})	$w_{A,LPP+}$ (cm^{-1})	ν_{SO} (cm^{-1})	ν_{LVM} (cm^{-1})
C024	9.25 (0.08)	-1.61 (0.06)	709.50 (0.11)	698.10 (1.01)
B738	11.21 (0.48)	0.29 (0.42)	710.32 (0.78)	—
C023	12.59 (0.36)	1.92 (0.39)	713.59 (0.42)	—
B982	13.96 (0.37)	2.64 (0.21)	712.91 (0.38)	—
C239	25.5 (2.8)	12.8 (3.1)	712.34 (0.42)	—
C144	22.19 (0.42)	8.52 (0.42)	715.26 (0.17)	—
C236	42.9 (11.9)	28.2 (9.5)	715.46 (0.74)	—
D299	9.08 (0.09)	-1.53 (0.07)	710.70 (0.06)	694.73 (0.13)
D260	11.01 (0.14)	1.90 (0.27)	713.47 (0.33)	697.70 (0.47)
D262	17.38 (0.41)	5.10 (0.30)	714.85 (0.82)	696.34 (0.24)
D273	37.11 (0.93)	4.09 (0.93)	714.63 (0.30)	694.63 (0.55)
D270	40.7 (1.3)	-2.22 (0.85)	718.58 (0.45)	—

TABLE V. The effect of above-band-gap UV illumination on the Raman frequencies and calculated carrier concentrations for samples B738, C023, B982, and C144. The parameters listed in columns 3 to 6 are, respectively, are the change in LPP+ peak frequency ($\Delta\nu_{LPP+}$) (on going from no UV illumination to illumination at intensity of 0.7 W/cm² or 4.5 W/cm²), the change in SO peak frequency ($\Delta\nu_{SO}$), the change in carrier concentration (ΔN), and the ratio $\Delta N/N_{avg}$ (where N_{avg} , the carrier concentration in the absence of UV illumination, is taken from Table II). Uncertainties are shown in parentheses after the parameter values.

Growth run	UV intensity (W/cm ²)	$\Delta\nu_{LPP+}$ (cm ⁻¹)	$\Delta\nu_{SO}$ (cm ⁻¹)	ΔN (10 ¹⁵ cm ⁻³)	ratio $\Delta N/N_{avg}$
B738	0.7	0.16 (0.12)	0.54 (0.60)	6.3 (4.8)	0.12 (0.09)
C023	0.7	0.07 (0.05)	0.49 (0.53)	2.7 (1.9)	0.034 (0.025)
B982	0.7	0.03 (0.06)	0.80 (0.50)	1.1 (2.2)	0.010 (0.021)
C144	0.7	0.15 (0.14)	0.49 (0.47)	5.6 (5.2)	0.027 (0.025)
B738	4.5	0.21 (0.17)	2.65 (0.75)	8.0 (6.6)	0.15 (0.13)
C023	4.5	0.05 (0.05)	0.19 (0.54)	2.1 (1.9)	0.026 (0.025)
B982	4.5	0.07 (0.08)	2.13 (0.72)	2.6 (3.1)	0.024 (0.028)
C144	4.5	0.01 (0.18)	0.01 (0.60)	0.4 (6.9)	0.002 (0.033)

TABLE VI. Effect of non-NW, matrix layer material on measured LPP+ frequencies and calculated carrier concentrations in samples B738 and B982. Results are shown for four measurements of B738 and six measurements of B982. The parameters are listed are the change in LPP+ peak frequency ($\Delta\nu_{LPP+}$) from each “as-grown: NWs + matrix” spectrum to the corresponding “difference: NWs only” spectrum, and the calculated change in carrier concentration (ΔN). Uncertainties are shown in parentheses after the parameter values.

Data set	$\Delta\nu_{LPP+}$ (cm^{-1})	ΔN (10^{15} cm^{-3})
B738(00,04)	−0.02 (0.20)	−0.7 (7.6)
B738(01,05)	−0.07 (0.23)	−2.5 (8.8)
B738(02,04)	−0.08 (0.18)	−3.0 (6.9)
B738(03,05)	+0.04 (0.20)	+1.6 (7.6)
B738(avg)	−0.03 (0.10)	−1.2 (3.9)
B982(34,40)	−0.25 (0.15)	−9.6 (5.9)
B982(35,41)	−0.12 (0.16)	−4.7 (5.9)
B982(36,40)	−0.37 (0.15)	−14.2 (5.8)
B982(37,41)	−0.21 (0.15)	−7.9 (5.8)
B982(38,40)	−0.28 (0.15)	−10.7 (5.7)
B982(39,41)	−0.14 (0.15)	−5.4 (5.8)
B982(avg)	−0.23 (0.10)	−8.8 (3.8)

Figure captions

1. The morphologies of the D series samples are shown at a distance of 27 mm from the center of each wafer. The morphology of an arbitrary location on sample B982 is shown for comparison. All micrographs were adjusted for consistent magnification, as indicated by the 5000 nm marker bar for the edge view and the 1000 nm marker bar for plan view.

2. Representative Raman spectra from GaN NW growth runs C024, B982, D262, and D273 are plotted in (a) the 500 cm^{-1} to 600 cm^{-1} range, with the peak frequencies of the $A_1(\text{TO})$, $E_1(\text{TO})$ and E_2^{high} modes and the Si substrate peak indicated by vertical dashed lines, and (b) the 650 cm^{-1} to 830 cm^{-1} range, with the peak frequencies of the surface optical (SO) and longitudinal phonon – plasmon (LPP+) modes in C024 indicated by vertical dashed lines.

3. Curve-fitting results are shown for a representative Raman spectrum from sample D262. The data points are shown as small squares, the fitted line shapes of the component lines are shown as dashed lines, and the overall fit, which is the sum of the component lines and a constant background, is shown as a solid line. The residual curve is shown as a solid line toward the bottom of the plot.

4. The calculated dependence of the carrier concentration (N) on LPP+ frequency ($\nu_{\text{LPP+}}$) from Eq. (4) is plotted as a solid curve. (Eq. (4) is displayed here for convenience.) Each data point represents the calculation result for a particular sample. The BC samples are indicated by

squares, and the D samples are indicated by circles. The error bars represent expanded uncertainties (95 % confidence intervals).

5. The carrier concentrations measured at six equally spaced locations on sample C239 are plotted as squares with error bars, and the corresponding LPP+ peak intensities are plotted as circles. The solid line connecting the peak intensities is included as a guide to the eye.

6. The dependence of carrier concentration (N) on Si cell temperature (T_{Si}) for the D samples is plotted. Each sample is represented by a circle and a vertical error bar. Sample D270 is seen to be an “outlier”, with higher than expected carrier concentration at $T_{Si} = 1175$ °C. The temperature dependence for the other four D samples was fit by an Arrhenius function with activation energy $E_a = 6.280 \pm 0.011$ eV, which is plotted as a dashed line.

7. The correlations of selected Raman line shape parameters with carrier concentration (N) or LPP+ frequency (ν_{LPP+}) are shown. Each data point represents one sample; the BC samples are indicated by squares, and the D samples are indicated by circles. (a) Correlation of the FWHM of the LPP+ line with N . (b) Correlation of the width asymmetry of the LPP+ line with N . (c) Correlation of the peak frequency of the SO mode (ν_{SO}) with N . (d) Correlation of ν_{SO} with ν_{LPP+} . The x-axis and y-axis ranges are chosen to be equal in this plot, and the dashed line is a linear fit to the shift of ν_{SO} with ν_{LPP+} , excluding the two highest- N samples.

8. Examples are shown of measured Raman spectra from “as-grown: NWs + matrix” and adjacent “scraped: matrix only” regions, and calculated “difference: NWs only” spectra, for (a)

sample B738, and (b) sample B982. To calculate each “difference: NWs only” spectrum, the “scraped” spectrum is weighted to null out the Si substrate peak in the difference spectrum.

9. Raman spectra of samples C144 (doped) and C024 (undoped) were measured in air and in microscope immersion oil. (a) Illustration of the subtraction procedure used to remove the oil-related Raman peaks: (bottom) immersion oil only spectrum, showing peaks due to oil constituents; (middle) measured spectrum of sample C144 in oil; (top) weighted difference spectrum with weighting chosen to best eliminate the oil-related peaks. (b) From bottom to top, spectra of sample C024 in air, C024 in oil (weighted difference), C144 in air, and C144 in oil (weighted difference). Note that the x-axis scale is expanded in part (b) to better display peak positions and line shapes.

10. Raman spectra measured for the (p,p) , (s,s) , (s,p) and (p,s) polarization geometries in sample D299 are plotted. (Polarization parallel or perpendicular to the plane of incidence is denoted p or s , respectively. The first label for each spectrum gives the incident polarization and the second label gives the scattered-light polarization.) Plotted intensities are multiplied by 6 to the right of the axis break, to better display the SO and LPP+ peaks.

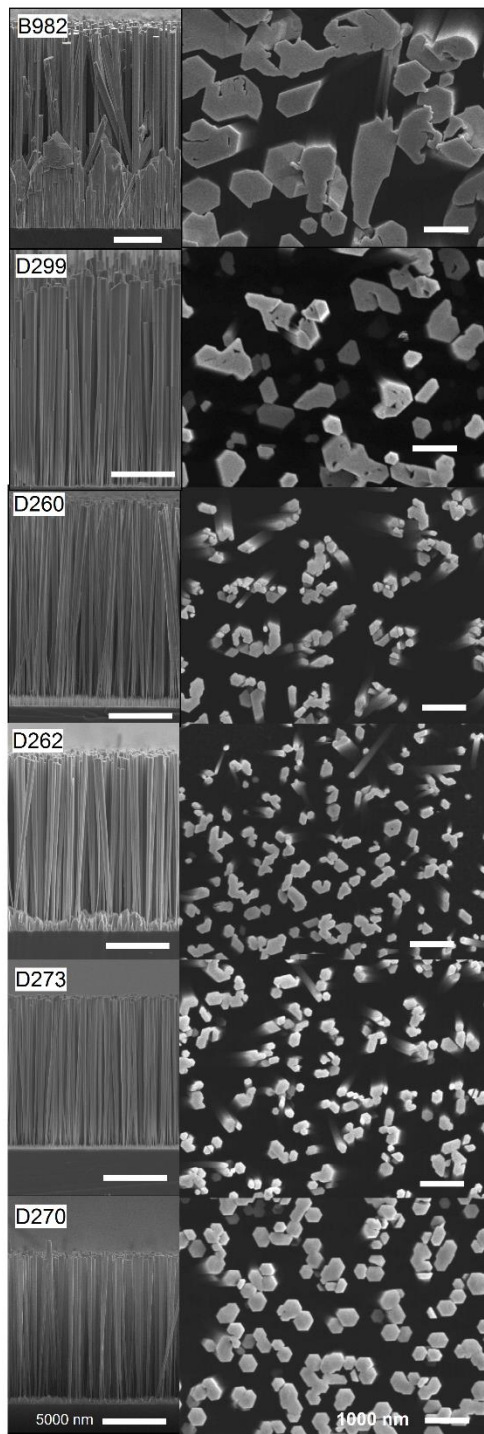


Fig. 1

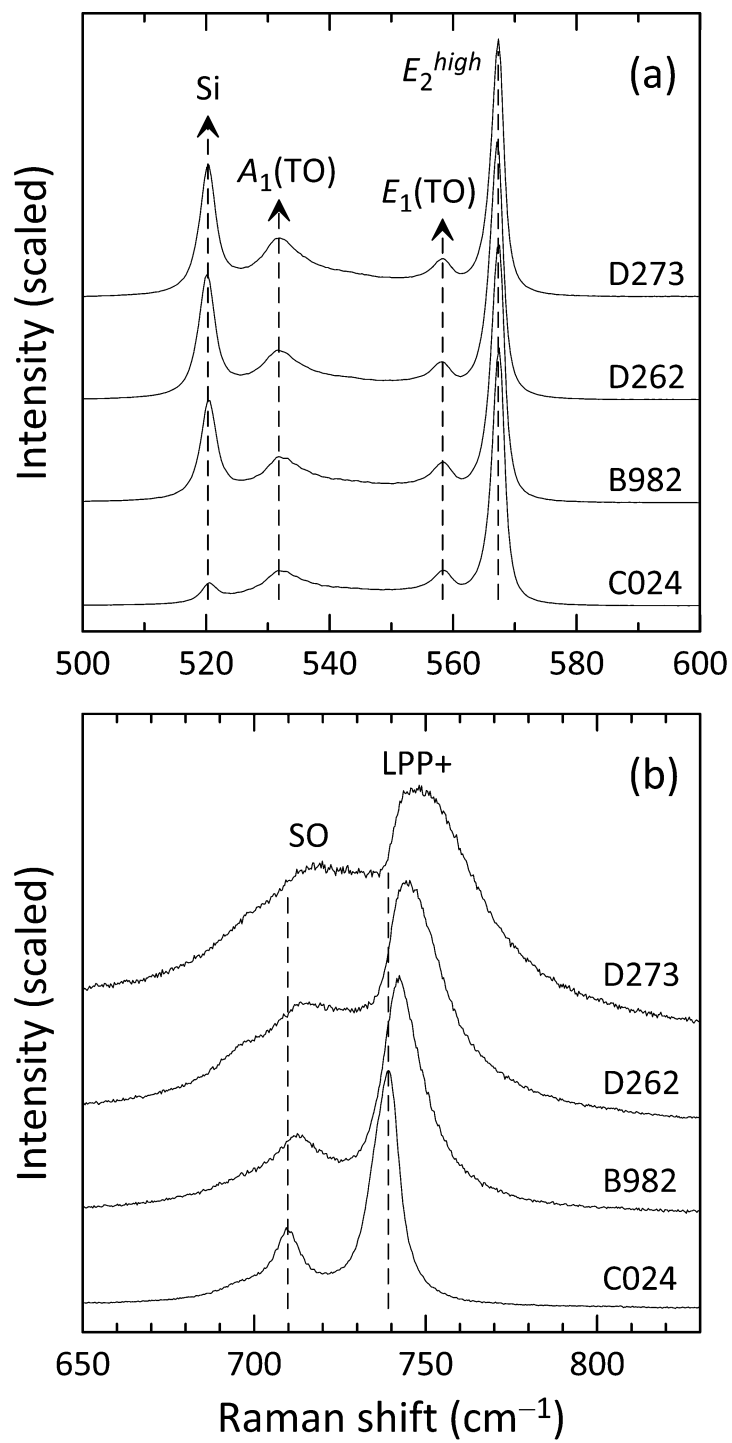


Fig. 2

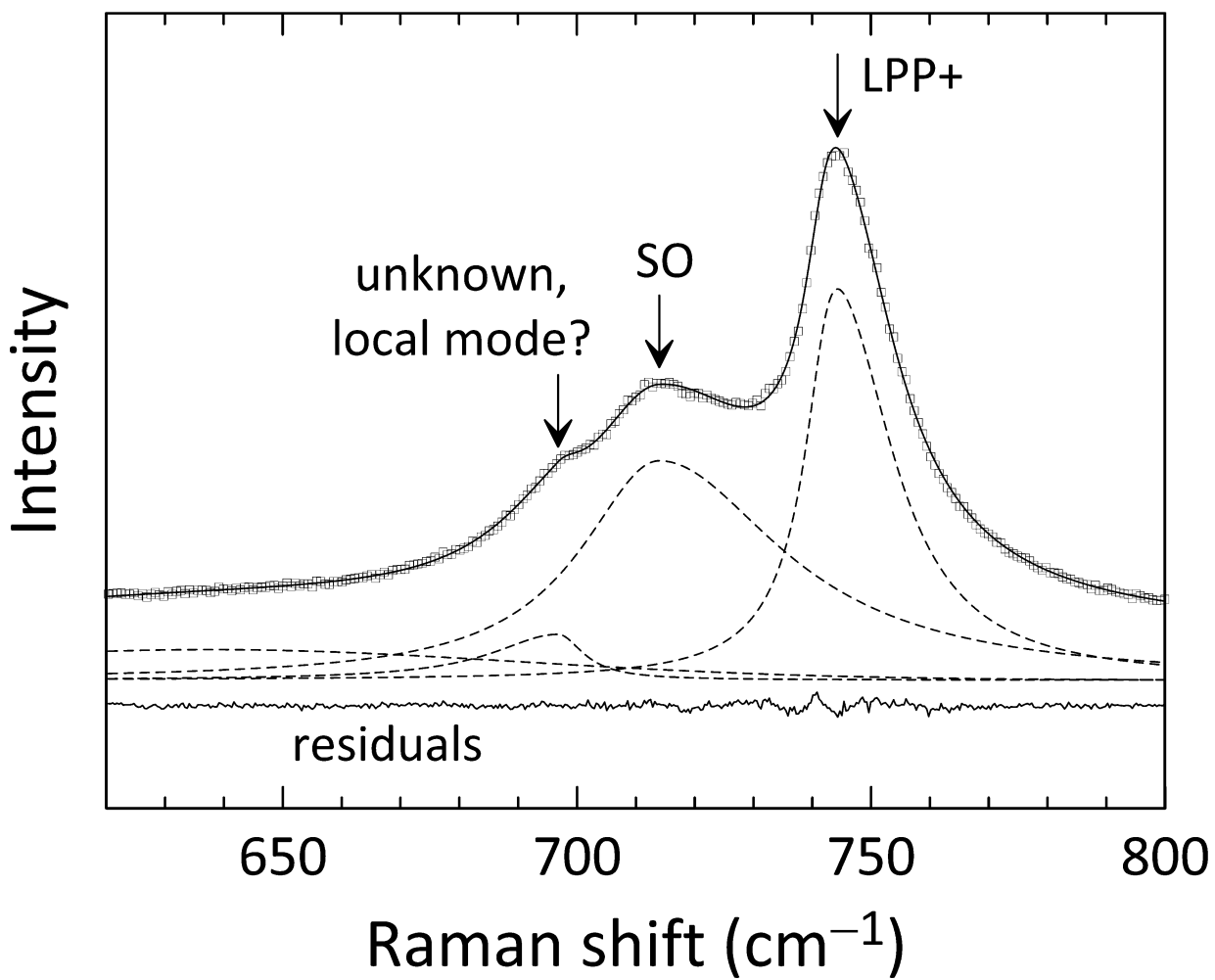


Fig. 3

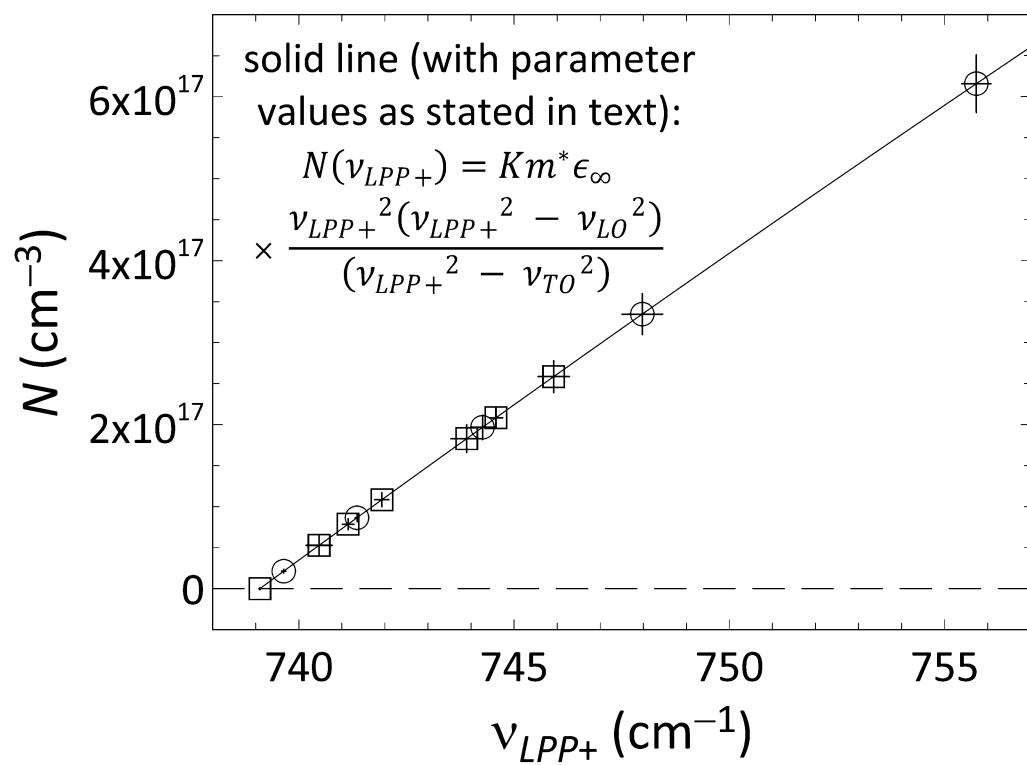


Fig. 4

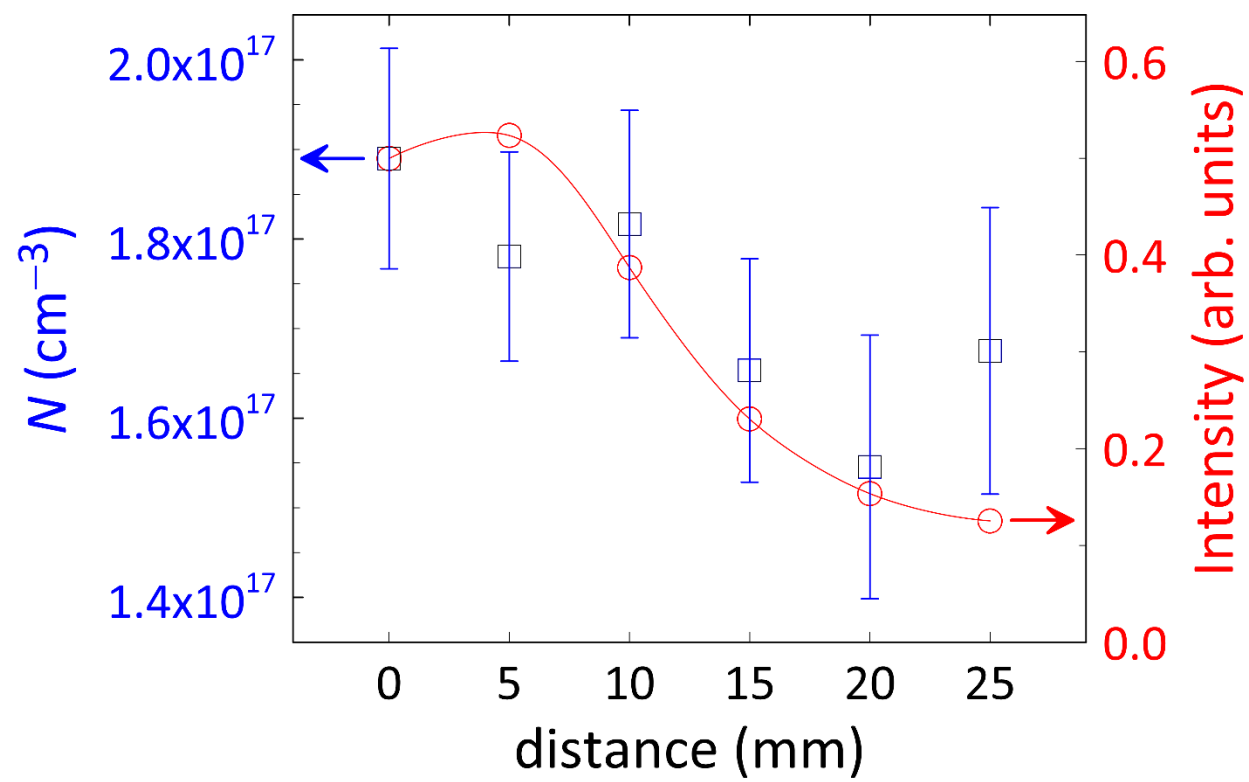


Fig. 5

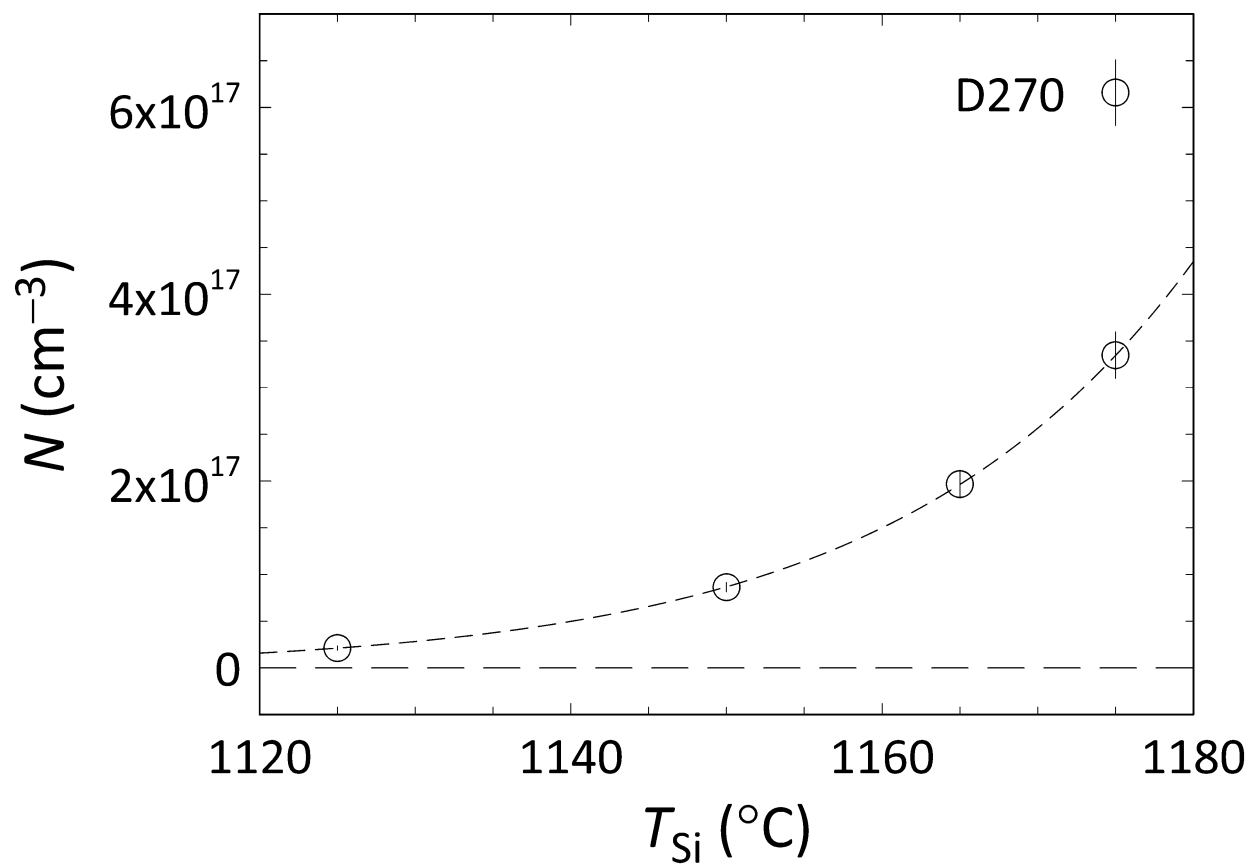


Fig. 6

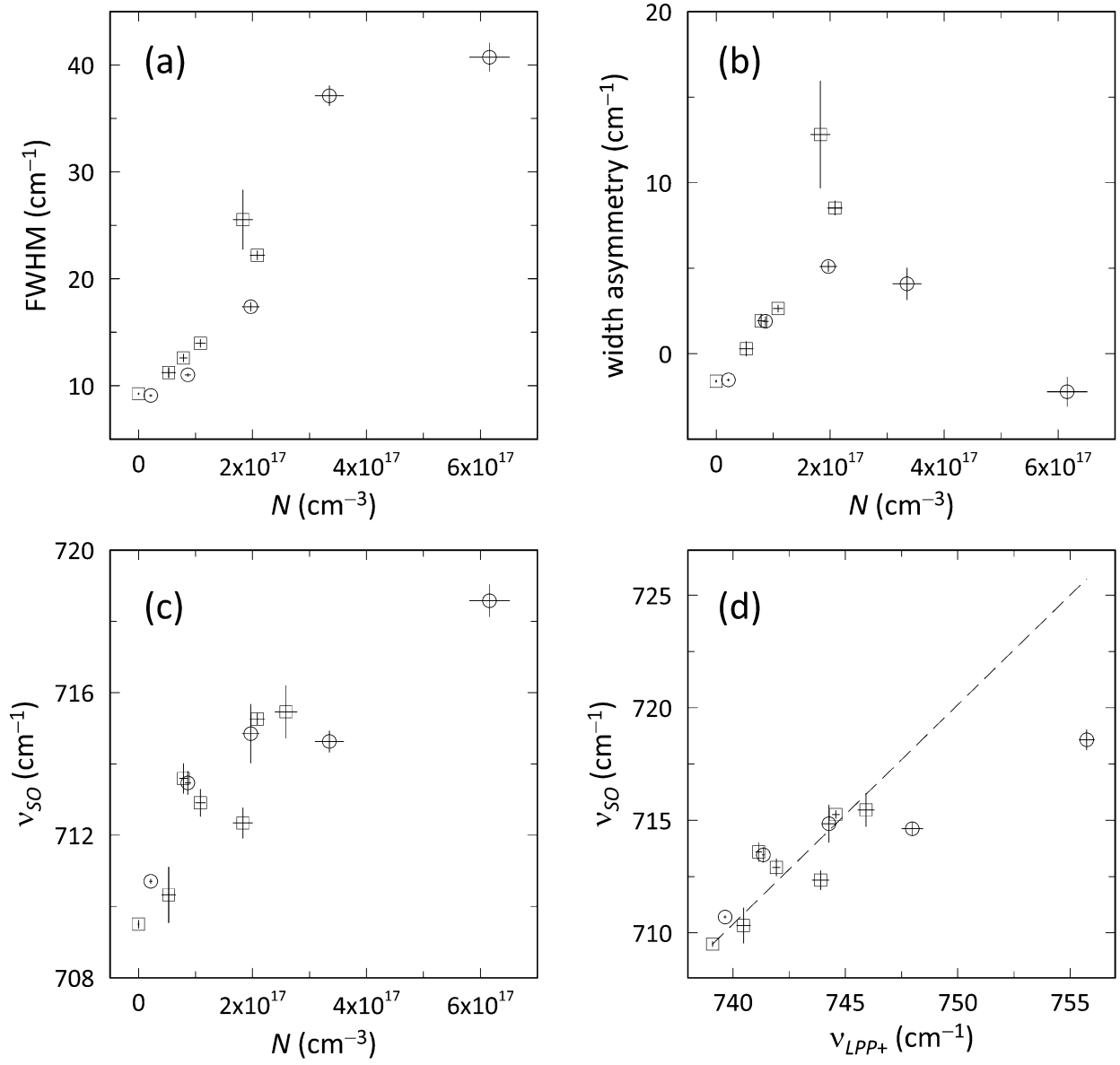


Fig. 7

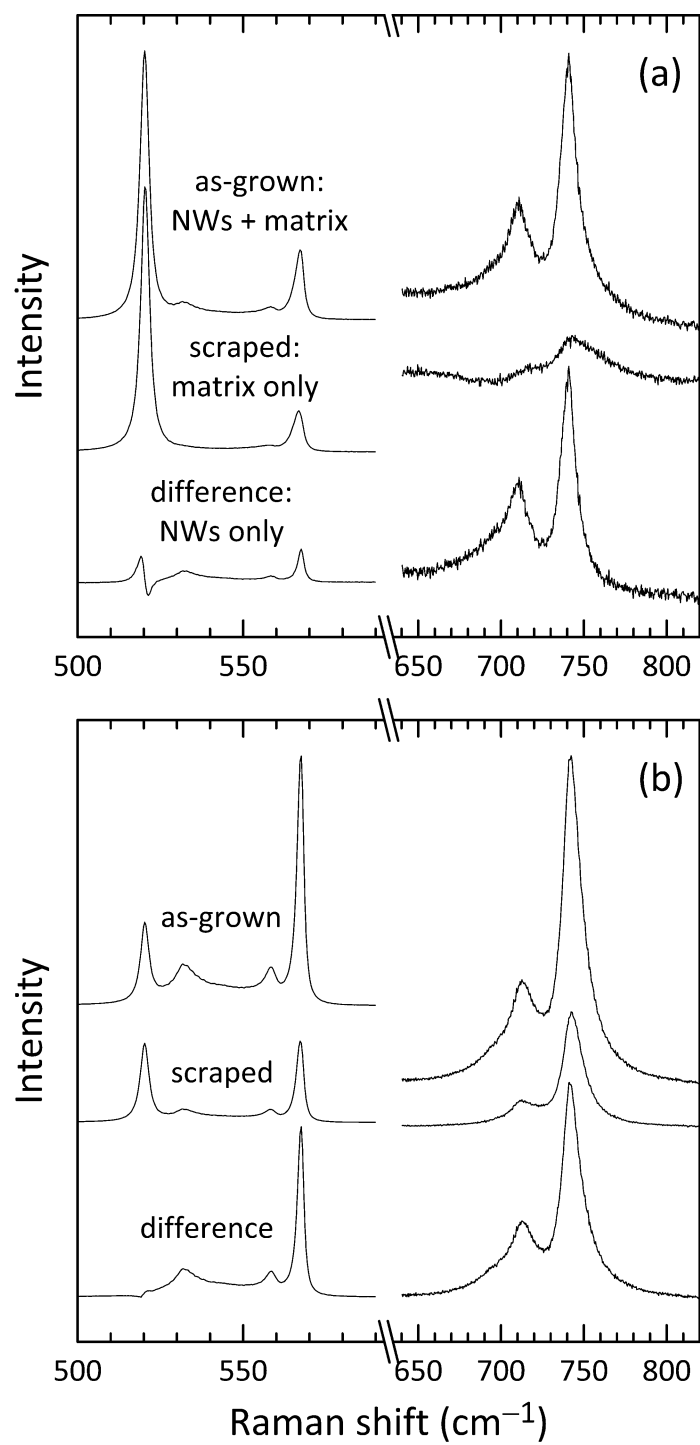


Fig. 8

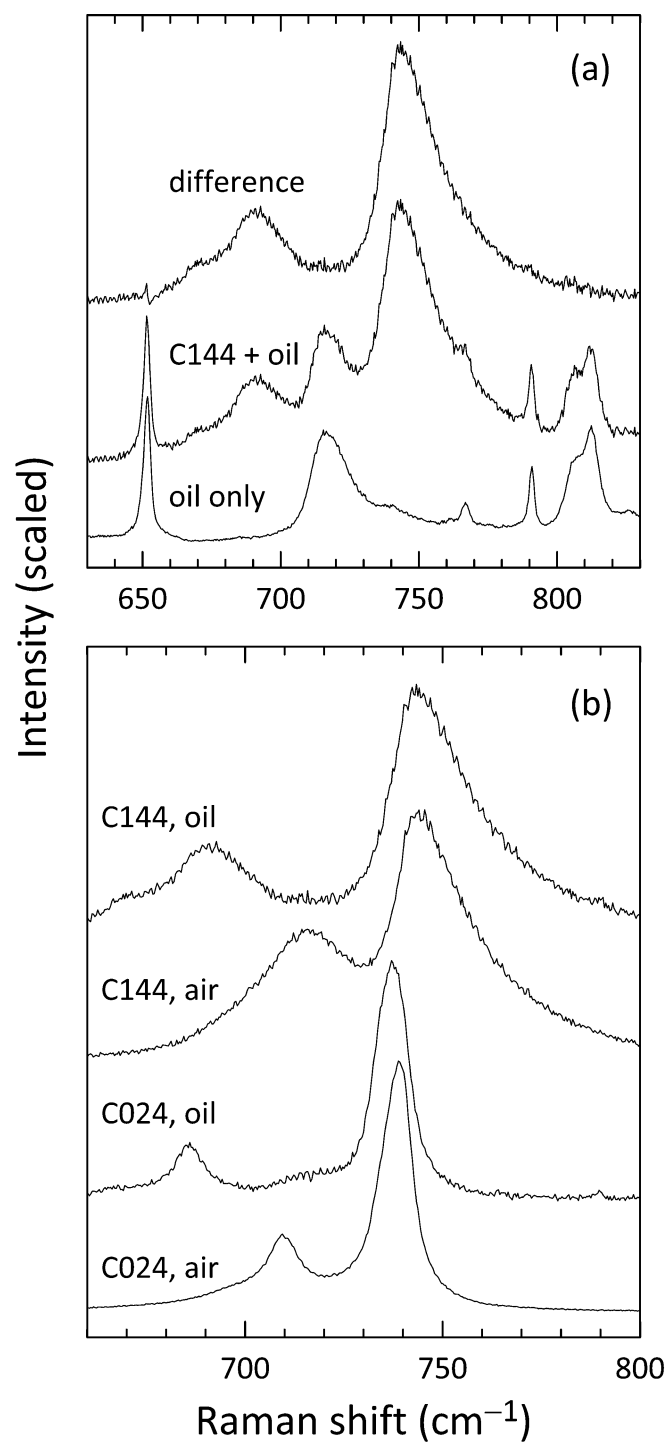


Fig. 9

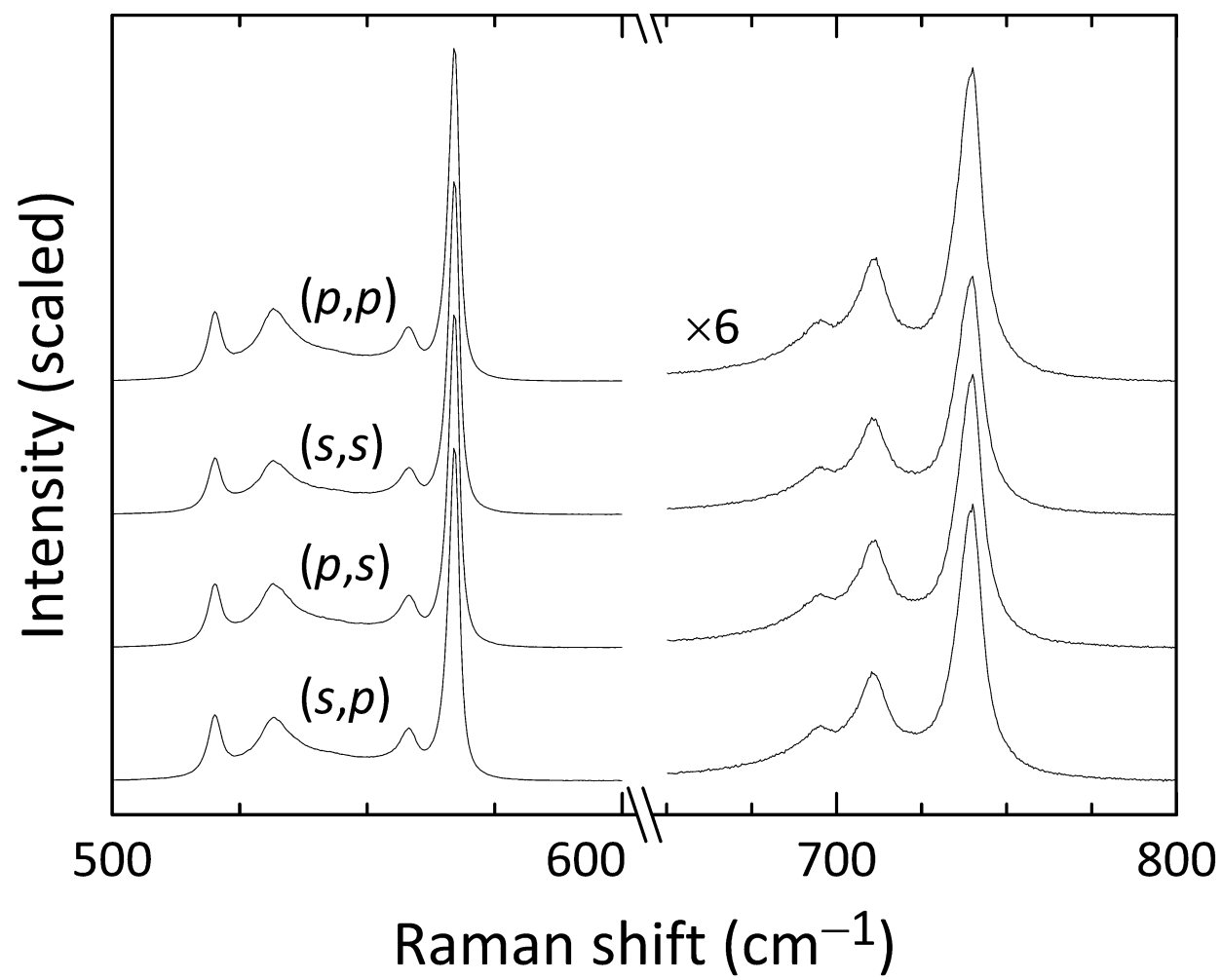


Fig. 10